J. Fluid Mech. (2021), *vol*. 917, A25, doi:10.1017/jfm.2021.257

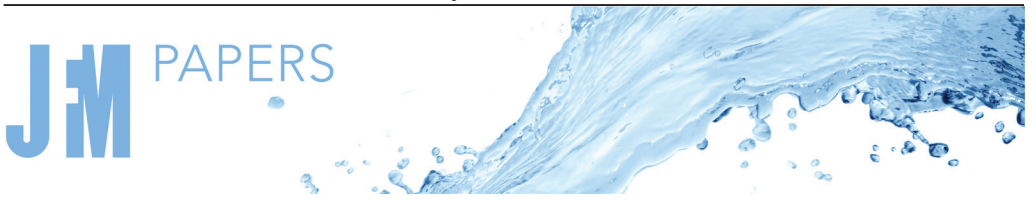

Unstable miscible displacements in radial flow with chemical reactions

Min Chan Kim[1], **Satyajit Pramanik**[2,†], **Vandita Sharma**[3] **and Manoranjan Mishra**[3]

[1]Department of Chemical Engineering, Jeju National University, Jeju 63243, Republic of Korea

[2]Department of Mathematics, Indian Institute of Technology Gandhinagar, Palaj, Gandhinagar 382355, India

[3]Department of Mathematics, Indian Institute of Technology Ropar, Rupnagar 140001, India

(Received 3 April 2020; revised 15 January 2021; accepted 16 March 2021)

The effects of the $A + B \rightarrow C$ chemical reaction on miscible viscous fingering in a radial source flow are analysed using linear stability theory and numerical simulations. This flow and transport problem is described by a system of nonlinear partial differential equations consisting of Darcy's law for an incompressible fluid coupled with nonlinear advection–diffusion–reaction equations. For an infinitely large Péclet number (Pe), the linear stability equations are solved using spectral analysis. Further, the numerical shooting method is used to solve the linearized equations for various values of Pe including the limit $Pe \rightarrow \infty$. In the linear analysis, we aim to capture various critical parameters for the instability using the concept of asymptotic instability, i.e. in the limit $\tau \rightarrow \infty$, where τ represents the dimensionless time. We restrict our analysis to the asymptotic limit Da^* $(= Da\tau) \rightarrow \infty$ and compare the results with the non-reactive case ($Da = 0$) for which $Da^* = 0$, where Da is the Damköhler number. In the latter case, the dynamics is controlled by the dimensionless parameter $R_{Phys} = -(R_A - \beta R_B)$. In the former case, for a fixed value of R_{Phys}, the dynamics is determined by the dimensionless parameter $R_{Chem} = -(R_C - R_B - R_A)$. Here, β is the ratio of reactants' initial concentration and R_A, R_B and R_C are the log-viscosity ratios. We perform numerical simulations of the coupled nonlinear partial differential equations for large values of Da. The critical values $R_{Phys,c}$ and $R_{Chem,c}$ for instability decrease with Pe and they exhibit power laws in Pe. In the asymptotic limit of infinitely large Pe they exhibit a power-law dependence on Pe ($R_{Chem,c} \sim Pe^{-1/2}$ as $Pe \rightarrow \infty$) in both the linear and nonlinear regimes.

Key words: fingering instability, porous media

† Email address for correspondence: satyajit.pramanik@iitgn.ac.in

1. Introduction

Flow and transport in porous media occur in a wide variety of situations such as in oil industries (Homsy 1987), carbon dioxide sequestration (Huppert & Neufeld 2014), contamination transport in subsurface aquifers (Welty, Kane & Kauffman 2003), lithium-ion batteries (Chung *et al.* 2014), hydrogeology (Cardenas *et al.* 2019) and biofilms (Davit *et al.* 2013), to name a few. When a less viscous fluid displaces a more viscous one in porous media, this unfavourable viscosity variation makes the system unstable and causes the displacing fluid to channel through the displaced one (Saffman & Taylor 1958). This instability, which is known as viscous fingering (VF), is a fundamental fluid mechanics problem which has important practical applications such as in secondary oil recovery (Homsy 1987), chromatography separation (Rana *et al.* 2019) and geothermal reservoir reinjection (Mcdowell, Zarrouk & Clarke 2016), to name a few. The first experimental study that reported this instability during the displacement of two miscible fluids in a porous medium was performed by Hill (1952). Several theoretical, computational and experimental studies have followed this seminal work to improve our understanding of the mechanism of VF and its controllability (Sharma *et al.* 2020).

The miscible VF occurring in the displacement driven by radial source flows has attracted many researchers due to the large number of laboratory experiments that are performed in radial Hele-Shaw cells as well as the important aspect of spatially dependent base velocity unlike the constant base velocity in rectilinear flow (e.g. Paterson 1981; Tan & Homsy 1987; Yortsos 1987; Sharma *et al.* 2020, and references therein). The effects of three-dimensional disturbances, velocity-induced dispersion and concentration-dependent diffusion were studied by solving the stability problems using both a linear stability theory and direct numerical simulations (Riaz & Meiburg 2003*a*,*b*; Riaz, Pankiewitz & Meiburg 2004). Pritchard (2004) revisited the radial fingering problem by considering double-diffusive effects due to heat and mass transfer and investigated the properties of each front contributing to the tendency of the flow instability by expanding the temperature and concentration disturbances as series of orthogonal functions. Linear stability analysis (LSA) and numerical simulations of VF during reinjection in geothermal reservoirs revealed that the key parameters governing the onset of VF instability and the finger structures are the Péclet number, the log-viscosity ratio and the permeability heterogeneity (Mcdowell *et al.* 2016). However, the effects of chemical reactions on the onset and the growth of the VF were not considered.

The effects of chemical reactions on VF instability have attracted the interest of several researchers (see De Wit (2016, 2020) for recent reviews). Experiments revealed that viscosity changing chemical reactions (Nagatsu *et al.* 2007) and precipitation reactions (Nagatsu *et al.* 2014) can induce VF in a radial Hele-Shaw cell. In precipitation reaction systems that produced metallic carbonate precipitations (e.g. $CaCO_3$, $BaCO_3$), the ratio of the reactants' concentration (i.e. the initial concentrations of the carbonate and the metallic ions), the species of the metallic ions and the injection flux played important roles in the pattern formation (Schuszter, Brau & De Wit 2016*a*,*b*; Schuszter & De Wit 2016). Experiments also revealed that the flow pattern controlled the morphology of barium carbonate ($BaCO_3$) precipitate particles (Schuszter & De Wit 2016). Very recent experiments captured that the interactions between chemical reactions and hydrodynamic instabilities controlled the morphology of the product and induced new dynamics phenomena (Balog *et al.* 2019; Escala *et al.* 2019).

Nonlinear numerical simulations of rectilinear displacements of $A + B \rightarrow C$ chemical reaction fronts captured various types of VF motions depending on different combinations

of physicochemical parameters (Gérard & De Wit 2009; Nagatsu & De Wit 2011; Nagatsu *et al.* 2014). Miscible displacements of reactive fronts in radial flow are scarcely explored theoretically. For example, a theoretical analysis of the properties of reaction–diffusion–advection fronts in the context of an $A + B \rightarrow C$ reactive miscible interface subjected to a passive radial advection (Brau, Schuszter & De Wit 2017) was followed by asymptotic solutions of this miscible reaction–diffusion–advection interface (Trevelyan & Walker 2018).

Recently, theoretical analyses discussed the effects of radial flow with chemical reaction on the solution thickness and dynamics of the reactive front without fingering instability (Brau & De Wit 2020; Tóth *et al.* 2020).

One of the first numerical studies exploring the effects of the reaction rate and the injection flux on the patterns of VF instability in a radial source flow of an $A + B \rightarrow C$ reactive miscible interface was recently presented by Sharma *et al.* (2019). They showed that when the two reactant fluids have the same viscosity, either the inner region or the outer region of the reaction front became unstable when the reaction produced a more or less viscous product. These clearly indicate that the theoretical and numerical studies exploring the effects of chemical reactions on miscible VF in radial flows are very limited and better understandings of the experimental observations await. Specifically, a systematic analysis for understanding the effects of both the hydrodynamics as well as chemistry that incorporates the effects of viscosity mismatch between the reactants remains unexplored.

In the present study, the effects of chemical reaction on the onset of VF during miscible displacement due to the radial source flow in a homogeneous porous medium were analysed with a linear stability theory based on the normal modes analysis and the results are compared with nonlinear simulations (NLS). The stability equations were formulated in a similarity domain and they are solved numerically and also analytically for some specific cases. We asked: How does the physical hydrodynamics in the form of the viscosity ratios of the two reactants, R_A and R_B, influence the reaction-induced fingering dynamics?

We restrict our stability analysis for the limiting case of $Da\tau \rightarrow \infty$, where Da is the Damköhler number and τ is the dimensionless time. They are defined in § 2.1.

Based on the results of the LSA, we extended the numerical work of Sharma *et al.* (2019) by considering such physical hydrodynamics effects on the instability patterns. We found that both the LSA and NLS predicted that the critical parameters for instability decay with Péclet number following power-law relations. A novel finding of our current study in this limiting case is that the instability of the system can be explained in the parameter space of two new mobility ratios, $R_{Phys} = -(R_A - \beta R_B)$ and $R_{Chem} = -(R_C - R_B - R_A)$. Here, R_C is the viscosity ratio associated with the product and β is the initial concentration ratio of reactant species A and B.

The organization of the paper is as follows. In § 2, the governing equations of the full nonlinear problem and the equations of the base state are presented. An analytic solution of the base-state concentration profiles are not attainable for arbitrary values of Da. However, a closed-form expression in terms of linear combinations of one of the reactants and the product concentration is presented with respect to a similarity variable. Further, we present analytic expressions for the base-state concentration profiles of all three species in the limits of no reaction and $Da\tau \rightarrow \infty$ for arbitrary values of Péclet number (Pe). In the asymptotic limit $Pe \gg 1$, these base-state profiles are further simplified and are shown graphically. The linearized perturbation equations are derived for performing the LSA in § 3 and their numerical solutions are discussed therein, followed by NLS in § 4.

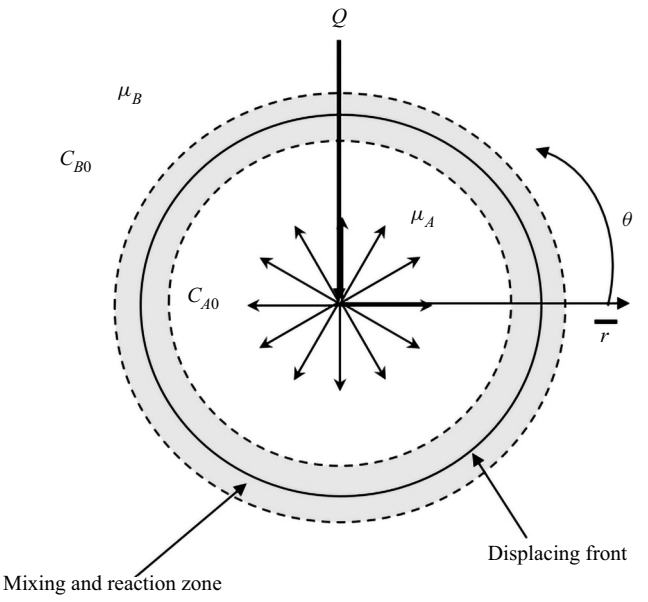

Figure 1. Schematic diagram of a reactive system $A + B \rightarrow C$ considered here.

Further the linear stability results are compared with the NLS in § 5 along with conclusions and implications for future research.

2. Mathematical model

We consider flow of incompressible, Newtonian fluids in a two-dimensional porous medium initially filled with a fluid having a species B dissolved in it and having a concentration C_{B0}. We inject a solution of the same solvent fluid and a solute A of concentration C_{A0} radially from a source at $r = 0$ with a constant flux Q as shown in figure 1. An irreversible second-order chemical reaction occurs between the two chemical species A and B, and produces another species C:

$$A + B \xrightarrow{k_r} C, \tag{2.1}$$

where k_r is the rate of the chemical reaction.

The governing equations for the conservation of mass and the conservation of momentum, and the advection–diffusion–reaction mass balance equations for the species are (De Wit 2016; Sharma *et al.* 2019)

$$\nabla \cdot \boldsymbol{U} = 0, \tag{2.2a}$$

$$\nabla P = -\frac{\mu}{K}\boldsymbol{U}, \tag{2.2b}$$

$$\frac{\partial C_A}{\partial t} + \boldsymbol{U} \cdot \nabla C_A = D_A \nabla^2 C_A - k_r C_A C_B, \tag{2.2c}$$

$$\frac{\partial C_B}{\partial t} + \boldsymbol{U} \cdot \nabla C_B = D_B \nabla^2 C_B - k_r C_A C_B, \tag{2.2d}$$

$$\frac{\partial C_C}{\partial t} + \boldsymbol{U} \cdot \nabla C_C = D_C \nabla^2 C_C + k_r C_A C_B, \tag{2.2e}$$

where $\boldsymbol{U} = (U, V)$ is the velocity vector, μ the viscosity, K the permeability, P the pressure, C_i the concentration of chemical species i and D_i the diffusion coefficient of the chemical species i ($i = A$, B and C).

2.1. *Non-dimensionalization*

For a radial flow, the equations of motion are best described in polar (r, θ) coordinates. We render the above system of equations dimensionless with the following scaling:

$$\tau = \frac{t}{2\pi K/Q}, \quad (u, v) = \frac{(U, V)}{Q/2\pi\sqrt{K}}, \tag{2.3a,b}$$

$$(a, b, c) = \frac{(C_A, C_B, C_C)}{C_{A0}}, \quad p = \frac{P}{\bar{\mu}Q/2\pi K}, \quad \mu = \frac{\tilde{\mu}}{\bar{\mu}}, \tag{2.4a–c}$$

where $\sqrt{K}$ is chosen as the characteristic length scale, such that $r \mapsto r/\sqrt{K}$. Here, $\bar{\mu}$ is the viscosity of the common solvent. Using these, the dimensionless equations can be written as

$$\frac{1}{r}\frac{\partial}{\partial r}(ru) + \frac{1}{r}\frac{\partial v}{\partial \theta} = 0, \tag{2.5a}$$

$$\frac{\partial p}{\partial r} = -\mu u, \tag{2.5b}$$

$$\frac{1}{r}\frac{\partial p}{\partial \theta} = -\mu v, \tag{2.5c}$$

$$\frac{\partial a}{\partial \tau} + \frac{1}{r}\frac{\partial (rua)}{\partial r} + \frac{1}{r}\frac{\partial (va)}{\partial \theta} = \frac{1}{Pe}\left[\frac{1}{r}\frac{\partial}{\partial r}\left(r\frac{\partial a}{\partial r}\right) + \frac{1}{r^2}\frac{\partial^2 a}{\partial \theta^2}\right] - Daab, \tag{2.5d}$$

$$\frac{\partial b}{\partial \tau} + \frac{1}{r}\frac{\partial (rub)}{\partial r} + \frac{1}{r}\frac{\partial (vb)}{\partial \theta} = \frac{1}{Pe}\left[\frac{1}{r}\frac{\partial}{\partial r}\left(r\frac{\partial b}{\partial r}\right) + \frac{1}{r^2}\frac{\partial^2 b}{\partial \theta^2}\right] - Daab, \tag{2.5e}$$

$$\frac{\partial c}{\partial \tau} + \frac{1}{r}\frac{\partial (ruc)}{\partial r} + \frac{1}{r}\frac{\partial (vc)}{\partial \theta} = \frac{1}{Pe}\left[\frac{1}{r}\frac{\partial}{\partial r}\left(r\frac{\partial c}{\partial r}\right) + \frac{1}{r^2}\frac{\partial^2 c}{\partial \theta^2}\right] + Daab. \tag{2.5f}$$

The dimensionless parameters appearing in (2.5) are the Péclet number Pe and the Damköhler number Da, which are defined as (Riaz & Meiburg 2003*a*,*b*; Trevelyan & Walker 2018)

$$Pe = \frac{Q}{2\pi D_A} \quad \text{and} \quad Da = \frac{2\pi k_r C_{A0} K}{Q}. \tag{2.6a,b}$$

The Péclet number represents the ratio of the advective transfer rate to the diffusive one, and the Damköhler number represents the ratio of the mass transfer time scale to the reaction time scale. To complete the above model, the viscosity variation with the concentration is assumed to follow an Arrhenius relation:

$$\mu(a, b, c) = \exp(R_A a + R_B b + R_C c), \tag{2.7}$$

where R_A, R_B and R_C are the log-viscosity ratios defined as

$$R_A = \ln\left(\frac{\mu(1, 0, 0)}{\mu(0, 0, 0)}\right), \quad R_B = \ln\left(\frac{\mu(0, 1, 0)}{\mu(0, 0, 0)}\right), \quad R_C = \ln\left(\frac{\mu(0, 0, 1)}{\mu(0, 0, 0)}\right). \tag{2.8a–c}$$

To focus on the effects of the chemical reaction only, Sharma *et al.* (2019) assumed $R_A = R_B = 0$, and therefore the physical hydrodynamic effects remained unexplored.

Note that the physicochemical effects on the viscosity profiles for the limiting cases of $R_A = 0$ and $\beta = 1$ are identical to those shown by Hejazi *et al.* (2010).

2.2. *Base state*

The above equations admit the following base-state axisymmetric solutions. The base-state velocity field is $(u_0, v_0) = (1/r, 0)$, whereas the base concentrations are governed by (Brau *et al.* 2017; Trevelyan & Walker 2018)

$$\frac{\partial a_0}{\partial \tau} + \left(1 - \frac{1}{Pe}\right)\frac{1}{r}\frac{\partial a_0}{\partial r} = \frac{1}{Pe}\frac{\partial^2 a_0}{\partial r^2} - Daa_0b_0, \tag{2.9a}$$

$$\frac{\partial b_0}{\partial \tau} + \left(1 - \frac{1}{Pe}\right)\frac{1}{r}\frac{\partial b_0}{\partial r} = \frac{1}{Pe}\frac{\partial^2 b_0}{\partial r^2} - Daa_0b_0, \tag{2.9b}$$

$$\frac{\partial c_0}{\partial \tau} + \left(1 - \frac{1}{Pe}\right)\frac{1}{r}\frac{\partial c_0}{\partial r} = \frac{1}{Pe}\frac{\partial^2 c_0}{\partial r^2} + Daa_0b_0, \tag{2.9c}$$

under the following conditions:

$$\left.\begin{aligned} a_0 - 1 = b_0 = c_0 = 0 \text{ at } r = 0, \\ a_0 = b_0 - \beta = c_0 = 0 \text{ as } r \to \infty, \end{aligned}\right\} \quad \forall\, \tau > 0, \tag{2.10a}$$

$$a_0 = b_0 - \beta = c_0 = 0 \text{ at } \tau = 0, \quad \forall\, r. \tag{2.10b}$$

Here, $\beta = C_{B0}/C_{A0}$ is the ratio of the reactants' initial concentration. Defining (see Appendix A for details)

$$\phi_0 = \frac{a_0 - b_0 + \beta}{1 + \beta} = a_0 + c_0, \tag{2.11}$$

the system of (2.9) can be reduced to the following single equation:

$$\frac{\partial \phi_0}{\partial \tau} + \left(1 - \frac{1}{Pe}\right)\frac{1}{r}\frac{\partial \phi_0}{\partial r} = \frac{1}{Pe}\frac{\partial^2 \phi_0}{\partial r^2}. \tag{2.12}$$

Further, the proper initial and boundary conditions are

$$\phi_0(r, 0) = 0, \quad \phi_0(0, \tau) = 1 \quad \text{and} \quad \phi_0(\infty, \tau) = 0. \tag{2.13a–c}$$

Therefore, the complete base-state concentration for both the reactants and product can be obtained as follows. (i) Solve the initial boundary value problem consisting of a linear advection–diffusion equation and Dirichlet conditions, given by (2.12) and (2.13*a–c*). (ii) Find the base-state concentration for one of the three species A, B and C. (iii) Subsequently, using the relations from (2.11) one can obtain the base-state concentration of the remaining two species. We will see in §§ 2.2.1 and 2.2.2 that for the limiting cases of $Da = 0$ and Da^* $(= Da\tau) \to \infty$, we have to solve only one initial boundary value problem for the unknown ϕ_0. For $Da^* < \infty$, one needs to solve two initial boundary value problems – one for the variable ϕ_0 and the other for one of the three species A, B and C – which is beyond the scope of this paper. Using the identity from (2.11), we

obtain

$$\beta a_0 + b_0 + (1+\beta)c_0 = \beta, \tag{2.14}$$

relating the base-state concentration of the species A, B and C. The gradient of the base-state log-viscosity is

$$\frac{\partial \ln \mu_0}{\partial r} = (R_A - \beta R_B)\frac{\partial \phi_0}{\partial r} + (R_C - R_B - R_A)\frac{\partial c_0}{\partial r}. \tag{2.15}$$

We introduce a similarity transformation $(r, \tau) \mapsto (\xi, \tau)$, where the similarity variable is defined as $\xi = r^2 Pe/(4\tau)$. Under this transformation, the steady state of ϕ_0 satisfies

$$\xi \frac{\mathrm{d}^2\phi_0}{\mathrm{d}\xi^2} + \left(\xi - \frac{Pe}{2} + 1\right)\frac{\mathrm{d}\phi_0}{\mathrm{d}\xi} = 0, \tag{2.16}$$

and yields the following similarity solution:

$$\phi_0(\xi) = \frac{\Gamma(Pe/2, \xi)}{\Gamma(Pe/2)} = \gamma(Pe/2, \xi). \tag{2.17}$$

Here, $\Gamma(\alpha, x) = \int_x^\infty t^{\alpha-1}\mathrm{e}^{-t}\mathrm{d}t$ is the upper incomplete gamma function, $\Gamma(\alpha)$ is the gamma function and $\gamma(\alpha, x)$ is the regularized upper incomplete gamma function. Combining (2.11) and (2.17), we obtain (Brau *et al.* 2017)

$$a_0 - b_0 = -\beta + (1+\beta)\gamma(Pe/2, \xi). \tag{2.18}$$

It is to be noted that the displacing front ($\xi = Pe/2$) is different from the reaction front (ξ_R), which can be obtained by setting $a_0 - b_0 = 0$ in (2.18) and solving for ξ yielding

$$\gamma(Pe/2, \xi_R) = \frac{\beta}{1+\beta}. \tag{2.19}$$

Note that (2.16) is similar to (41) of Tan & Homsy (1987) barring that $Pe/2$ in the former is replaced by Pe in the latter. Since we write the base-state concentration of the species in terms of $\phi_0(\xi)$ and our LSA is performed in terms of the similarity variable ξ, we will see in § 3 that the stiff nature of the stability equations becomes a problem for large Pe as explained by Tan & Homsy (1987). Therefore, following Tan & Homsy (1987) we present our LSA for three different cases of Pe: (i) general values of Pe up to $O(10)$, (ii) moderate Pe ($Pe \gg 1$) and (iii) asymptotically large Pe ($Pe \to \infty$).

For $Pe \gg 1$, (2.17) reduces to

$$\phi_0(\zeta) = \tfrac{1}{2}\mathrm{erfc}(\zeta) + O(Pe^{-1/2}), \tag{2.20}$$

where $\zeta = (\xi - Pe/2)/\sqrt{Pe}$ and hence $\zeta = 0$ is the displacing front. For $Pe \geqslant 20$, (2.20) approximates (2.17) quite well (Tan & Homsy 1987; Kim 2012). The reaction front ζ_R, at which we have $a_0(\zeta_R) = b_0(\zeta_R)$, can be approximated as

$$\zeta_R = \mathrm{erfc}^{-1}\left(\frac{2\beta}{1+\beta}\right). \tag{2.21}$$

The physical and chemical fronts, i.e. the displacing and the reaction fronts, coincide if and only if $\beta = 1$.

2.2.1. *Non-reactive case ($Da = 0$)*

In the non-reactive case ($Da = 0$), no product is formed ($c_0 = 0$) and we have $Da^* = 0$. Therefore, from (2.11) and (2.15) we obtain

$$(a_0, b_0) = (\phi_0, \beta(1 - \phi_0)), \tag{2.22a}$$

$$\frac{\partial \ln \mu_0}{\partial r} = (R_A - \beta R_B)\frac{\partial \phi_0}{\partial r}. \tag{2.22b}$$

Because in this limit the chemical reaction plays no role in the viscosity distribution, we define $R_{Phys} = -(R_A - \beta R_B)$, and this limit of Da^* will be used to analyse the case of non-reactive displacements (Kim 2012).

2.2.2. *Case of $Da^* \to \infty$*

For the limiting cases of $Da^* \to \infty$, such as $CaCO_3$ and $BaCO_3$ precipitation systems considered in Schuszter & De Wit (2016), the two reactants do not coexist, i.e. $a_0(\xi \geqslant \xi_R) = 0$ and $b_0(\xi < \xi_R) = 0$. Therefore, the base concentration fields and the gradient of the log-viscosity can be obtained as

$$(a_0, b_0, c_0) = \begin{cases} ((1+\beta)\phi_0 - \beta, 0, \beta(1-\phi_0)) & \text{for } \xi \leqslant \xi_R, \\ (0, \beta - (1+\beta)\phi_0, \phi_0) & \text{for } \xi > \xi_R, \end{cases} \tag{2.23a}$$

$$\frac{\partial \ln \mu_0}{\partial r} = \begin{cases} -(R_{Phys} - \beta R_{Chem})\dfrac{\partial \phi_0}{\partial r} & \text{for } \xi \leqslant \xi_R, \\ -(R_{Phys} + R_{Chem})\dfrac{\partial \phi_0}{\partial r} & \text{for } \xi > \xi_R, \end{cases} \tag{2.23b}$$

where $R_{Chem} = -(R_C - R_B - R_A)$.

The base concentration profiles given in (2.20) and (2.23*a*) are plotted in figure 2 with respect to the transformed self-similar variable ζ for $\beta < 1$, $\beta = 1$ and $\beta > 1$. This figure depicts, as expected by the construction of the new variable ζ, that the displacing front, $\zeta = 0$, is universal with respect to β. It also confirms that the reaction front depends on β and it is different from the displacing front for $\beta \neq 1$. When the reactant species A and B have the same initial concentration ($\beta = 1$), the reaction front is the same as the displacing front and the product concentration becomes symmetric about this front (see figure 2*b*). On the other hand, when one of the reactant species is more concentrated than the other (i.e. $\beta > 1$ or $\beta < 1$), their diffusive fluxes are different, which results in an asymmetry behaviour of the displacing front. For $\beta \neq 1$, the reaction front and hence greater amount of product are situated in the region that is rich in the less concentrated species. Figures 2(*a*) and 2(*c*) depict that the reaction front is situated in the B-rich and A-rich regions, respectively, for $\beta < 1$ and $\beta > 1$. Depending upon these base-state concentration profiles, the VF instability can occur when the less viscous reactant A pushes the more viscous product C, or less viscous product C displaces the more viscous reactant B, or both. In the following sections, we present LSA as well as NLS for understanding these reactive VF instability cases.

Since $\partial\phi_0/\partial r$ is always negative regardless of Da^*, (2.23*b*) suggests that the instabilities of the inner and the outer interfaces of the product depend on the sign of $R_{Phys} - \beta R_{Chem}$ and $R_{Phys} + R_{Chem}$, respectively. In short, we expect inward and outward fingers at the

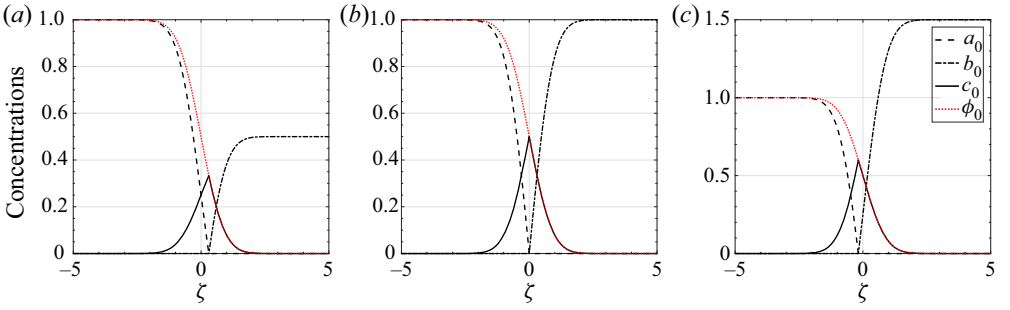

Figure 2. Base-state concentrations $a_0(\zeta)$, $b_0(\zeta)$ and $c_0(\zeta)$ along with $\phi_0(\zeta)$ are plotted in the limiting case of $Da^* \to \infty$ for different values of $\beta < 1$, $\beta = 1$ and $\beta > 1$: (*a*) $\beta = 0.5$, (*b*) $\beta = 1$ and (*c*) $\beta = 1.5$.

inner and outer interfaces of the product when the inequalities

$$R_{Chem} < R_{Phys}/\beta, \tag{2.24a}$$

$$R_{Chem} > -R_{Phys} \tag{2.24b}$$

are satisfied, respectively. These stability conditions are equivalent to $R_C > R_A(1+\beta)/\beta$ and $R_C < R_B(1+\beta)$, respectively. Note that both the inequalities hold simultaneously only when $R_{Phys} > 0$. In such cases, both the inward and outward fingers may appear when $-R_{Phys} < R_{Chem} < R_{Phys}/\beta$, or equivalently, $R_A(1+\beta)/\beta < R_C < R_B(1+\beta)$.

3. Linear stability analysis

3.1. *Stability equations*

Under the LSA, we introduce infinitesimal disturbances around the base-state solutions, such that $u = u_0 + u_1$, $v = v_0 + v_1$, $p = p_0 + p_1$, $a = a_0 + a_1$, $b = b_0 + b_1$, $c = c_0 + c_1$, where the subscripts '0' and '1' correspond to the base state and the disturbance quantities, respectively. The resulting perturbed equations are

$$\frac{1}{r}\frac{\partial}{\partial r}(ru_1) + \frac{1}{r}\frac{\partial v_1}{\partial \theta} = 0, \tag{3.1a}$$

$$\frac{\partial p_1}{\partial r} = -\mu_0 u_1 - \frac{1}{r}\left[\left(\frac{\partial \mu}{\partial a}\right)_{(a_0,b_0,c_0)} a_1 + \left(\frac{\partial \mu}{\partial b}\right)_{(a_0,b_0,c_0)} b_1 + \left(\frac{\partial \mu}{\partial c}\right)_{(a_0,b_0,c_0)} c_1\right], \tag{3.1b}$$

$$\frac{1}{r}\frac{\partial p_1}{\partial \theta} = -\mu_0 v_1, \tag{3.1c}$$

$$\frac{\partial a_1}{\partial \tau} + \frac{1}{r}\frac{\partial a_1}{\partial r} + \frac{\partial a_0}{\partial r}u_1 = \frac{1}{Pe}\left[\frac{1}{r}\frac{\partial}{\partial r}\left(r\frac{\partial a_1}{\partial r}\right) + \frac{1}{r^2}\frac{\partial^2 a_1}{\partial \theta^2}\right] - Da(a_0 b_1 + a_1 b_0), \tag{3.1d}$$

$$\frac{\partial b_1}{\partial \tau} + \frac{1}{r}\frac{\partial b_1}{\partial r} + \frac{\partial b_0}{\partial r}u_1 = \frac{1}{Pe}\left[\frac{1}{r}\frac{\partial}{\partial r}\left(r\frac{\partial b_1}{\partial r}\right) + \frac{1}{r^2}\frac{\partial^2 b_1}{\partial \theta^2}\right] - Da(a_0 b_1 + a_1 b_0), \tag{3.1e}$$

$$\frac{\partial c_1}{\partial \tau} + \frac{1}{r}\frac{\partial c_1}{\partial r} + \frac{\partial c_0}{\partial r}u_1 = \frac{1}{Pe}\left[\frac{1}{r}\frac{\partial}{\partial r}\left(r\frac{\partial c_1}{\partial r}\right) + \frac{1}{r^2}\frac{\partial^2 c_1}{\partial \theta^2}\right] + Da(a_0 b_1 + a_1 b_0). \tag{3.1f}$$

The corresponding boundary conditions are

$$ru_1 \to 0, \quad a_1 \to 0, \quad b_1 \to 0 \quad \text{and} \quad c_1 \to 0 \text{ as } r \to 0, \tag{3.2a}$$

$$u_1 \to 0, \quad a_1 \to 0, \quad b_1 \to 0 \quad \text{and} \quad c_1 \to 0 \text{ as } r \to \infty. \tag{3.2b}$$

Eliminating pressure and the azimuthal velocity component, the linear stability equations (3.1*a*)–(3.1*c*) reduce to

$$\frac{\partial^2 \psi_1}{\partial r^2} + \left(\frac{1}{r} + R_A \frac{\partial a_0}{\partial r} + R_B \frac{\partial b_0}{\partial r} + R_C \frac{\partial c_0}{\partial r}\right) \frac{\partial \psi_1}{\partial r} + \frac{1}{r^2} \frac{\partial^2 \psi_1}{\partial \theta^2}$$

$$= -\frac{1}{r^2} \frac{\partial^2}{\partial \theta^2} (R_A a_1 + R_B b_1 + R_C c_1), \tag{3.3}$$

where $\psi_1 = ru_1$. In the spirit of ϕ_0 defined in (2.11), we define

$$\phi_1 = \frac{a_1 - b_1}{1 + \beta} = a_1 + c_1 = -\frac{b_1 + c_1}{\beta}, \tag{3.4}$$

such that (3.1*d*)–(3.1*f*) can be reduced to a single advection–diffusion equation:

$$\frac{\partial \phi_1}{\partial \tau} + \frac{1}{r} \frac{\partial \phi_1}{\partial r} + \frac{\partial \phi_0}{\partial r} u_1 = \frac{1}{Pe} \left[\frac{1}{r} \frac{\partial}{\partial r} \left(r \frac{\partial \phi_1}{\partial r}\right) + \frac{1}{r^2} \frac{\partial^2 \phi_1}{\partial \theta^2}\right]. \tag{3.5}$$

The proper boundary conditions associated with (3.3) and (3.5) are

$$\psi_1 = \phi_1 = 0 \text{ at } r = 0, \tag{3.6a}$$

$$\psi_1 \to 0 \quad \text{and} \quad \phi_1 \to 0 \text{ as } r \to \infty. \tag{3.6b}$$

From (3.4), we get the following auxiliary relation:

$$\beta a_1 + b_1 + (1 + \beta) c_1 = 0. \tag{3.7}$$

Using the similarity transformation introduced in § 2, $(r, \tau) \mapsto (\xi, \tau)$, where the similarity variable is defined as $\xi = Pe(r^2/4\tau)$, (3.3) and (3.5) are transformed into

$$\frac{\partial}{\partial \xi} \left(\xi \frac{\partial \psi_1}{\partial \xi}\right) + \left(R_A \frac{\partial a_0}{\partial \xi} + R_B \frac{\partial b_0}{\partial \xi} + R_C \frac{\partial c_0}{\partial \xi}\right) \xi \frac{\partial \psi_1}{\partial \xi} + \frac{1}{4\xi} \frac{\partial^2 \psi_1}{\partial \theta^2}$$

$$= -\frac{1}{4\xi} \frac{\partial^2}{\partial \theta^2} (R_A a_1 + R_B b_1 + R_C c_1), \tag{3.8a}$$

$$\tau \frac{\partial \phi_1}{\partial \tau} = \mathcal{L}_\xi \phi_1 + \frac{1}{4\xi} \frac{\partial^2 \phi_1}{\partial \theta^2} - \frac{1}{2} Pe \frac{\mathrm{d}\phi_0}{\mathrm{d}\xi} \psi_1, \tag{3.8b}$$

respectively. Here, the differential operator $\mathcal{L}_\xi$ is defined as

$$\mathcal{L}_\xi = \frac{\partial}{\partial \xi} \left(\xi \frac{\partial}{\partial \xi}\right) + \left(\xi - \frac{Pe}{2}\right) \frac{\partial}{\partial \xi}. \tag{3.9}$$

For the limiting case of $Pe \gg 1$, (3.8) become

$$\frac{\partial^2 \psi_1^*}{\partial \zeta^2} + \left(R_A \frac{\partial a_0}{\partial \zeta} + R_B \frac{\partial b_0}{\partial \zeta} + R_C \frac{\partial c_0}{\partial \zeta}\right) \frac{\partial \psi_1^*}{\partial \zeta} + \frac{1}{Pe} \frac{\partial^2 \psi_1^*}{\partial \theta^2}$$

$$= -\frac{1}{Pe} \frac{\partial^2}{\partial \theta^2} (R_A^* a_1 + R_B^* b_1 + R_C^* c_1) + O(Pe^{-1/2}), \tag{3.10a}$$

$$2\tau \frac{\partial \phi_1}{\partial \tau} = \mathcal{L}_\zeta \phi_1 + \frac{1}{Pe} \frac{\partial^2 \phi_1}{\partial \theta^2} - \frac{\mathrm{d}\phi_0}{\mathrm{d}\zeta} \psi_1^* + O(Pe^{-1/2}), \tag{3.10b}$$

where

$$\mathcal{L}_\zeta = \frac{\partial^2}{\partial \zeta^2} + 2\zeta \frac{\partial}{\partial \zeta} \tag{3.11}$$

and $\psi_1^* = \psi_1\sqrt{Pe}$, $R_A^* = R_A\sqrt{Pe}$, $R_B^* = R_B\sqrt{Pe}$ and $R_C^* = R_C\sqrt{Pe}$.

In the remainder of this section, we discuss linear stability in the limit $Da^* \to \infty$ (see Appendix B for the non-reactive case, i.e. $Da^* = 0$). In this limit, both the advection and the diffusion terms remain significant in (3.1*d*)–(3.1*f*), provided

$$a_0 b_1 + a_1 b_0 = 0. \tag{3.12}$$

Recall that for $Da^* \to \infty$, we have $a_0(\xi \geqslant \xi_R) = 0$ and $b_0(\xi < \xi_R) = 0$. Combining this with (3.12), we obtain $a_1(\xi \geqslant \xi_R) = 0$ and $b_1(\xi < \xi_R) = 0$. Hence, using (3.4), the concentration disturbance fields can be obtained as

$$(a_1, b_1, c_1) = \begin{cases} ((1+\beta)\phi_1, 0, -\beta\phi_1) & \text{for } 0 \leqslant \xi \leqslant \xi_R \\ (0, -(1+\beta)\phi_1, \phi_1) & \text{for } \xi > \xi_R. \end{cases} \tag{3.13}$$

In this limit, (3.8*a*) becomes

$$\frac{\partial}{\partial \xi}\left(\xi \frac{\partial \psi_1}{\partial \xi}\right) - (R_{Phys} - \beta R_{Chem}) \frac{\mathrm{d}\phi_0}{\mathrm{d}\xi} \xi \frac{\partial \psi_1}{\partial \xi} + \frac{1}{4\xi}\frac{\partial^2 \psi_1}{\partial \theta^2}$$

$$= (R_{Phys} - \beta R_{Chem}) \frac{1}{4\xi}\frac{\partial^2 \phi_1}{\partial \theta^2} \quad \text{for } \xi \leqslant \xi_R, \tag{3.14a}$$

$$\frac{\partial}{\partial \xi}\left(\xi \frac{\partial \psi_1}{\partial \xi}\right) - (R_{Phys} + R_{Chem}) \frac{\mathrm{d}\phi_0}{\mathrm{d}\xi} \xi \frac{\partial \psi_1}{\partial \xi} + \frac{1}{4\xi}\frac{\partial^2 \psi_1}{\partial \theta^2}$$

$$= (R_{Phys} + R_{Chem}) \frac{1}{4\xi}\frac{\partial^2 \phi_1}{\partial \theta^2} \quad \text{for } \xi > \xi_R. \tag{3.14b}$$

Similarly, (3.10*a*) becomes

$$\frac{\partial^2 \psi_1^*}{\partial \zeta^2} - (R_{Phys} - \beta R_{Chem}) \frac{\mathrm{d}\phi_0}{\mathrm{d}\zeta} \frac{\partial \psi_1^*}{\partial \zeta} + \frac{1}{Pe}\frac{\partial^2 \psi_1^*}{\partial \theta^2}$$

$$= (R_{Phys}^* - \beta R_{Chem}^*) \frac{1}{Pe}\frac{\partial^2 \phi_1}{\partial \theta^2} + O(Pe^{-1/2}) \quad \text{for } \zeta \leqslant \zeta_R, \tag{3.15a}$$

$$\frac{\partial^2 \psi_1^*}{\partial \zeta^2} - (R_{Phys} + R_{Chem}) \frac{\mathrm{d}\phi_0}{\mathrm{d}\zeta} \frac{\partial \psi_1^*}{\partial \zeta} + \frac{1}{Pe}\frac{\partial^2 \psi_1^*}{\partial \theta^2}$$

$$= (R_{Phys}^* + R_{Chem}^*) \frac{1}{Pe}\frac{\partial^2 \phi_1}{\partial \theta^2} + O(Pe^{-1/2}) \quad \text{for } \zeta > \zeta_R. \tag{3.15b}$$

Here, $R_{Phys}^* = R_{Phys}\sqrt{Pe}$ and $R_{Chem}^* = R_{Chem}\sqrt{Pe}$. The corresponding boundary conditions associated with (3.8*b*) (or (B2) for $Da^* = 0$) and (3.14) are

$$\psi_1 = \phi_1 = 0 \text{ at } \xi = 0, \tag{3.16a}$$

$$\psi_1 \to 0 \quad \text{and} \quad \phi_1 \to 0 \text{ as } \xi \to \infty, \tag{3.16b}$$

whereas the boundary conditions associated with (3.10*b*) (or (B3) for $Da^* = 0$) and (3.15) are

$$\psi_1^* = 0 \quad \text{and} \quad \phi_1 = 0 \text{ at } \zeta = -\sqrt{Pe}/2, \tag{3.17a}$$

$$\psi_1^* \to 0 \quad \text{and} \quad \phi_1 \to 0 \text{ as } \zeta \to \infty. \tag{3.17b}$$

3.2. *Normal mode analysis*

Since the coefficients of (3.8*b*) (or (B2) for $Da^* = 0$) and (3.14) are independent of τ and θ, under the normal mode analysis (Tan & Homsy 1987), the perturbation quantities ϕ_1 and ψ_1 are expressed as

$$\phi_1(\xi, \theta, \tau) = \Phi(\xi) \mathrm{e}^{\mathrm{i}n\theta} \tau^{\sigma}, \tag{3.18a}$$

$$\psi_1(\xi, \theta, \tau) = \Psi(\xi) \mathrm{e}^{\mathrm{i}n\theta} \tau^{\sigma}, \tag{3.18b}$$

where n is the azimuthal wavenumber and growth exponent σ is defined as $\tau(\partial\phi_1/\partial\tau) = \sigma\phi_1$. Using this normal mode decomposition, (3.8*b*) becomes

$$\sigma\Phi = \mathcal{L}_{\xi}\Phi - \frac{n^2}{4\xi}\Phi - \frac{1}{2}Pe\frac{\mathrm{d}\phi_0}{\mathrm{d}\xi}\Psi, \tag{3.19}$$

associated with the equation for the velocity disturbance field:

$$\begin{aligned}&\frac{\mathrm{d}}{\mathrm{d}\xi}\left(\xi\frac{\mathrm{d}\Psi}{\mathrm{d}\xi}\right) - (R_{Phys} - \beta R_{Chem})\frac{\mathrm{d}\phi_0}{\mathrm{d}\xi}\xi\frac{\mathrm{d}\Psi_1}{\mathrm{d}\xi} - \frac{n^2}{4\xi}\Psi \\ &\quad = -(R_{Phys} - \beta R_{Chem})\frac{n^2}{4\xi}\Phi \quad \text{for } \xi \leqslant \xi_R,\end{aligned} \tag{3.20a}$$

$$\begin{aligned}&\frac{\mathrm{d}}{\mathrm{d}\xi}\left(\xi\frac{\mathrm{d}\Psi}{\mathrm{d}\xi}\right) - (R_{Phys} + R_{Chem})\frac{\mathrm{d}\phi_0}{\mathrm{d}\xi}\xi\frac{\mathrm{d}\Psi_1}{\mathrm{d}\xi} - \frac{n^2}{4\xi}\Psi \\ &\quad = -(R_{Phys} + R_{Chem})\frac{n^2}{4\xi}\Phi \quad \text{for } \xi > \xi_R.\end{aligned} \tag{3.20b}$$

The boundary conditions corresponding to (3.19)–(3.20) are

$$\Psi \to 0 \quad \text{and} \quad \Phi \to 0, \ \text{as } \xi \to \pm\infty. \tag{3.21}$$

Similarly, for $Pe \gg 1$, we can apply normal mode analysis as discussed below. Since the coefficients of the stability (3.10*b*), (B3) and (3.15) are independent of τ and θ, the normal mode decomposition of ψ_1^* reads

$$\psi_1^*(\zeta, \theta, \tau) = \Psi^*(\zeta) \mathrm{e}^{\mathrm{i}n\theta} \tau^{\sigma}, \tag{3.22}$$

where $\Psi(\xi)$ and $\Psi^*(\zeta)$ satisfy $\Psi^* = \Psi\sqrt{Pe}$. Using this normal mode decomposition for ψ_1^*, along with that for ϕ_1 given in (3.18*a*), the stability equations become

$$\sigma\Phi = \frac{1}{2}\left(\mathcal{L}_{\zeta} - \frac{n^2}{Pe}\right)\Phi - \frac{1}{2}\frac{\mathrm{d}\phi_0}{\mathrm{d}\zeta}\Psi^*, \tag{3.23}$$

associated with

$$\frac{\mathrm{d}^2\Psi^*}{\mathrm{d}\zeta^2} - (R_{Phys} - \beta R_{Chem})\frac{\mathrm{d}\phi_0}{\mathrm{d}\zeta}\frac{\mathrm{d}\Psi^*}{\mathrm{d}\zeta} - \frac{n^2}{Pe}\Psi^* = -\frac{n^2}{Pe}(R^*_{Phys} - \beta R^*_{Chem})\Phi \quad \text{for } \zeta \leqslant \zeta_R, \tag{3.24a}$$

$$\frac{\mathrm{d}^2\Psi^*}{\mathrm{d}\zeta^2} - (R_{Phys} + R_{Chem})\frac{\mathrm{d}\phi_0}{\mathrm{d}\zeta}\frac{\mathrm{d}\Psi^*}{\mathrm{d}\zeta} - \frac{n^2}{Pe}\Psi^* = -\frac{n^2}{Pe}(R^*_{Phys} + R^*_{Chem})\Phi \quad \text{for } \zeta > \zeta_R. \tag{3.24b}$$

The boundary conditions corresponding to (3.23)–(3.24) are

$$\Psi^* \to 0 \quad \text{and} \quad \Phi \to 0, \text{ as } \zeta \to \pm\infty. \tag{3.25}$$

As mentioned in the introduction, contrary to its rectilinear counterpart, theoretical and numerical studies exploring the effects of chemical reactions for miscible VF in radial flows await understanding. In a rectilinear flow, the onset time of instability is captured in terms of frozen time-dependent growth rate using a quasi-steady-state approximation (Hejazi *et al.* 2010). It is widely accepted that a quasi-steady-state approximation has its own limitation in the linear stability theory (Kim & Choi 2011) and the same can be overcome by performing the stability analysis in a suitably defined similarity domain (Ben, Demekhin & Chang 2002). In the present study, we have used a similarity transformation and have focused on capturing the critical parameters for the instability using asymptotic instability criterion ($\tau \to \infty$) as follows. From (3.18*a*) and (3.18*b*), it is clear that the perturbations decay to zero as $\tau \to \infty$ when $\sigma < 0$; whereas they grows to infinity as $\tau \to \infty$ when $\sigma > 0$. A system is said to be asymptotically stable in the former case, and asymptotically unstable in the latter case (Drazin & Reid 2004; Chandrasekhar 2013). Therefore, the critical parameters corresponding to the linear stability theory are computed for $Da^*(= Da\tau) \to \infty$. We demarcate the parameter space as stable and unstable corresponding to which $\sigma < 0$ and $\sigma > 0$, respectively. The boundary between these two regions indicates the critical parameters for the onset of instability. Furthermore, a radial flow is significantly different from a rectilinear flow and the LSAs in these two configurations have some critical differences (Tan & Homsy 1987). For brevity, we do not present any direct comparison between rectilinear and radial flows.

3.2.1. *Shooting method*

In general, in order to integrate the stability (3.19)–(3.20), a trial value of the eigenvalue σ and that of $\mathrm{d}\Psi/\mathrm{d}\xi$, Θ and $\mathrm{d}\Theta/\mathrm{d}\xi$ at $\xi = \xi_R$ are assumed properly for given values of R, n and Pe (Kim 2018). Since the boundary conditions (3.16) are all homogeneous, the value of Ψ at $\xi = \xi_R$ can be assigned arbitrarily. This procedure is based on the shooting method in which the boundary value problem is transformed into the initial value problem. The initial value problem is integrated numerically using the fourth-order Runge–Kutta method. Numerical shooting is done on both sides of the reaction front, $\xi = \xi_R$, i.e. $0 \leqslant \xi \leqslant \xi_R$ and $\xi_R \leqslant \xi < \infty$, such that the boundary conditions (3.16) are satisfied respectively in these two regions. On the right of the injection front, we enforce the boundary conditions (3.16*b*) to satisfy on a fictitious outer boundary. We use Newton–Raphson iteration to iteratively correct the trial values of σ, $\mathrm{d}\Psi/\mathrm{d}\xi$, Θ and $\mathrm{d}\Theta/\mathrm{d}\xi$ at $\xi = \xi_R$ until the linear stability equations satisfy the boundary conditions (3.16) within a relative tolerance of 10^{-10}. Then by increasing the fictitious outer boundary step by step, the above integration is repeated. Finally, the value of σ is decided through extrapolation.

3.2.2. *Spectral analysis*

Following Pritchard (2004) and Kim (2012), here we obtain an analytic solution for the limiting case of $Pe \to \infty$, $R_{Phys} \ll 1$ and $R_{Chem} \ll 1$, but finite $R^*_{Phys} = R_{Phys}\sqrt{Pe}$ and $R^*_{Chem} = R_{Chem}\sqrt{Pe}$. Under the Sturm–Liouville theory (Al-Gwaiz 2008), Φ can be expressed as

$$\Phi(\zeta) = \sum_{i=0}^{\infty} A_i \alpha_i \phi_i(\zeta), \tag{3.26}$$

where $\phi_i(\zeta)$ are the eigenfunctions of the Sturm–Liouville equation,

$$\mathcal{L}_\zeta \phi_i = -2\lambda_i \phi_i. \tag{3.27}$$

The solutions of the above equation are weighted ith Hermite polynomials:

$$\phi_i(\zeta) = \mathrm{e}^{-\zeta^2} H_i(\zeta) \quad \text{and} \quad i = (\lambda_i - 1) = 0, 1, 2, \ldots \tag{3.28}$$

Here, the normalization factors α_i are

$$\alpha_i = (\sqrt{\pi} 2^i \mathcal{G}(i+1))^{-1/2}, \quad i = (\lambda_i - 1) = 0, 1, 2, \ldots \tag{3.29}$$

Combining (B5) (or equations (3.24)) with (3.26), it can be shown that $\Psi^*(\zeta)$ follows a series expansion with the same coefficients as $\Phi(\zeta)$, and the former can be expressed as

$$\Psi^*(\zeta) = \sum_{i=0}^{\infty} A_i \alpha_i \psi_i(\zeta), \tag{3.30}$$

where ψ_i can be obtained by solving ($R_{Phys}, R_{Chem} \ll 1$)

$$\frac{\mathrm{d}^2 \psi_i^-}{\mathrm{d}\zeta^2} - k^2 \psi_i^- = -k^2 (R^*_{Phys} - \beta R^*_{Chem}) \mathrm{e}^{-\zeta^2} H_i(\zeta) \quad \text{for } \zeta \leqslant \zeta_R, \tag{3.31a}$$

$$\frac{\mathrm{d}^2 \psi_i^+}{\mathrm{d}\zeta^2} - k^2 \psi_i^+ = -k^2 (R^*_{Phys} + R^*_{Chem}) \mathrm{e}^{-\zeta^2} H_i(\zeta) \quad \text{for } \zeta > \zeta_R, \tag{3.31b}$$

such that

$$\psi_i = \begin{cases} \psi_i^-, & \zeta \leqslant \zeta_R \\ \psi_i^+, & \zeta > \zeta_R \end{cases} \quad \text{and} \tag{3.32a}$$

$$\lim_{\zeta \to \zeta_R +} \psi_i^+ = \psi_i^-(\zeta_R). \tag{3.32b}$$

Here, $k = n/\sqrt{Pe}$ is the scaled wavenumber. We analytically solve the second-order ordinary differential equation (C5) (or (3.31)) associated with the following boundary conditions: $\psi_i \to 0$ as $\zeta \to \pm\infty$. The solutions are summarized in Appendix C. Substituting the above solutions into (3.23), we obtain an eigenvalue problem:

$$\sigma \boldsymbol{a} = \boldsymbol{B}\boldsymbol{a}, \tag{3.33}$$

where

$$B_{mn} = -\frac{1}{2}(2\lambda_m + k^2)\delta_{mn} + \frac{1}{2\sqrt{\pi}} C_{mn}, \quad m, n = 0, 1, 2, \ldots, \tag{3.34a}$$

$$C_{mn} = \int_{-\infty}^{\infty} \alpha_m \alpha_n \phi_m(\zeta) \psi_n(\zeta) \mathrm{d}\zeta, \quad m, n = 0, 1, 2, \ldots, \tag{3.34b}$$

$$\boldsymbol{a} = [A_0, A_1, A_2, \ldots]^{\mathrm{T}}. \tag{3.34c}$$

The growth rate of the perturbed quantities is bounded from above by the largest eigenvalues of $\boldsymbol{B}$, i.e.

$$\sigma = \max\{\mathrm{eig}(\boldsymbol{B})\}. \tag{3.35}$$

Furthermore, we apply the numerical shooting method, discussed in § 3.2.1, to solve (3.23)–(3.24) and the corresponding boundary conditions (3.25).

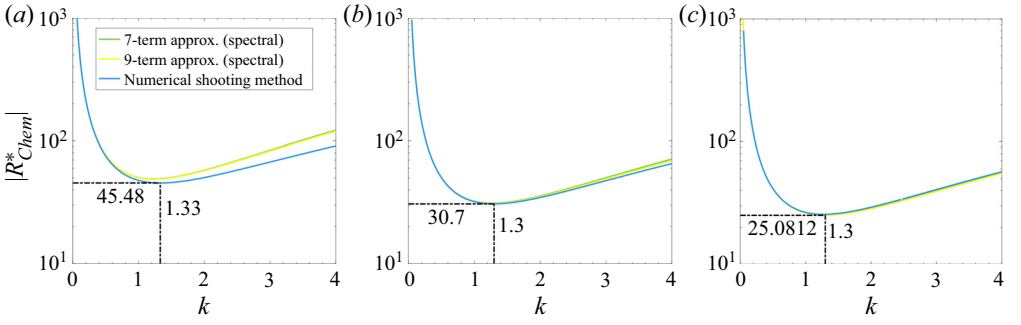

Figure 3. Neutral stability curves obtained using spectral analysis (7-term and 9-term approximations) and numerical shooting method for $R^*_{Phys} = 0$, $Pe \to \infty$, $Da^* \to \infty$, (*a*) $\beta = 1/2$, (*b*) $\beta = 1$ and (*c*) $\beta = 2$. The region above (below) each curve corresponds to the region of instability (stability). The values of $|R^*_{Chem}|$ and k corresponding to the lowest point of the curve representing the numerical shooting method denote the critical values for the instability. These are denoted by $|R^*_{Chem,c}|$ and k_c and are shown by horizontal and vertical dashed-dotted lines, respectively.

3.3. *Critical conditions for linear instability*

The critical conditions for the linearly unstable modes are determined by analysing the neutral stability curves. For example, the critical values of R^*_{Chem} and k (i.e. $R^*_{Chem,c}$ and k_c) are obtained from the neutral curves plotted in the R^*_{Chem}–k plane. For the limiting case of $Pe \to \infty$, the neutral stability curves obtained by solving (3.23)–(3.25) using both the spectral analysis and the numerical shooting method are plotted in figure 3. This figure depicts that the critical value $|R^*_{Chem,c}|$ decreases as β increases (e.g. $|R^*_{Chem,c}| = 45.48$, 30.70 and 21.93 for $\beta = 1/2$, 1 and 2, respectively), but the critical wavenumber k_c does not change significantly with β and remains near 1.30. Recalling $R^*_{Chem} = R_{Chem}\sqrt{Pe}$ and $k = n/\sqrt{Pe}$, we approximate for $\beta = 1$, $R_{Chem} = 30.70/Pe^{1/2}$ and $n_c = 1.30Pe^{1/2}$ as $Pe \to \infty$. Figure 3 also reveals that the numerical shooting method is in very good agreement with the spectral solutions.

Next, we analyse the effects of β on the the critical values $R^*_{Chem,c}$ in terms of R^*_{Phys} as shown in figure 4. This figure reveals that $R^*_{Chem,c}$ has non-trivial dependences on β and R^*_{Phys}. First, we discuss when the initial concentrations of both the reactants are the same, i.e. $\beta = 1$. For $\beta = 1$, we have $\zeta_R = 0$. In this case, if R^*_{Chem} has a negative value, we denote the eigenfunctions as $\psi_{i,n}$ and hence (3.31) can be reduced to

$$\frac{\mathrm{d}^2\psi^-_{i,n}}{\mathrm{d}\zeta^2} - k^2\psi^-_{i,n} = -k^2\left(R^*_{Phys} - \left|R^*_{Chem}\right|\right)\mathrm{e}^{-\zeta^2}H_i(\zeta) \quad \text{for } \zeta \leqslant 0, \tag{3.36a}$$

$$\frac{\mathrm{d}^2\psi^+_{i,n}}{\mathrm{d}\zeta^2} - k^2\psi^+_{i,n} = -k^2\left(R^*_{Phys} + \left|R^*_{Chem}\right|\right)\mathrm{e}^{-\zeta^2}H_i(\zeta) \quad \text{for } \zeta > 0. \tag{3.36b}$$

Similarly, for positive values of R^*_{Chem} we denote the eigenfunctions as $\psi_{i,p}$ and from (3.31) one can obtain

$$\frac{\mathrm{d}^2\psi^-_{i,p}}{\mathrm{d}\zeta^2} - k^2\psi^-_{i,p} = -k^2\left(R^*_{Phys} + \left|R^*_{Chem}\right|\right)\mathrm{e}^{-\zeta^2}H_i(\zeta) \quad \text{for } \zeta \leqslant 0, \tag{3.37a}$$

$$\frac{\mathrm{d}^2\psi^+_{i,p}}{\mathrm{d}\zeta^2} - k^2\psi^+_{i,p} = -k^2\left(R^*_{Phys} - \left|R^*_{Chem}\right|\right)\mathrm{e}^{-\zeta^2}H_i(\zeta) \quad \text{for } \zeta > 0. \tag{3.37b}$$

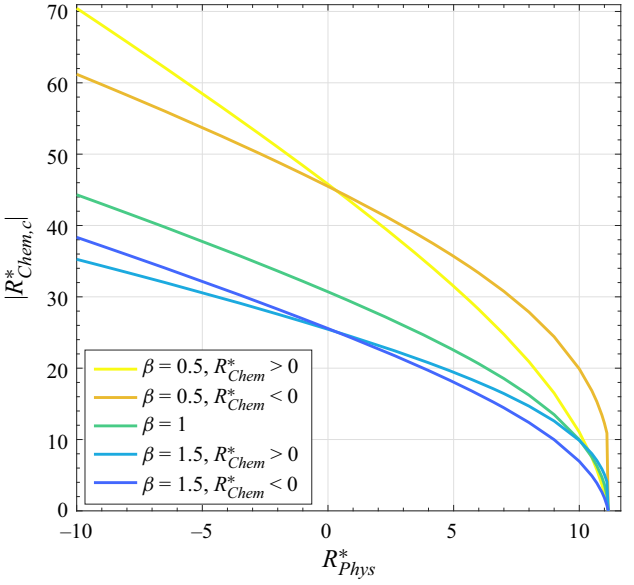

Figure 4. Variation of the critical parameter $R^*_{Chem,c}$ with R^*_{Phys} obtained from spectral analysis for $Da^* \to \infty$, $Pe \to \infty$ and different values of β. For $\beta = 1$, positive and negative $R^*_{Chem,c}$ are identical. For $\beta \neq 1$, positive and negative $R^*_{Chem,c}$ are not only different, but also have a non-trivial dependence on the sign of R^*_{Phys}.

For the odd-mode instabilities, i.e. $H_i(-\zeta) = -H_i(\zeta)$, $\psi^-_{i,n} = -\psi^+_{i,p}$, $\psi^-_{i,p} = -\psi^+_{i,n}$ (see Appendix D for further details), and therefore C_{mn} of the negative R^*_{Chem} and the positive R^*_{Chem} have opposite sign. In this case the stability condition is strongly dependent on the sign of R^*_{Chem}. Kim (2014) reported that the even modes are more unstable than the odd modes. For the even-mode instabilities, i.e. $H_i(-\eta) = H_i(\eta)$, $\psi^+_{i,n} = \psi^-_{i,p}$ and $\psi^-_{i,n} = \psi^+_{i,p}$, and therefore C_{mn} of the negative R^*_{Chem} and the positive R^*_{Chem} cases are the same. In other words, for the limiting case of $\beta = 1$, the critical conditions are independent of the sign of R^*_{Chem}, as shown in figure 4.

The amount of product generated is proportional to β. Therefore, irrespective of the signs of R_{Phys} and R_{Chem}, the displacements become more unstable as β increases. On the contrary, for fixed values of β, the fingering dynamics exhibits more non-trivial dependencies on R_{Phys} and R_{Chem}. As expected, the dynamics is strongly dependent on the signs of both of these dimensionless parameters. First, we consider the case for which the physical front is neutrally stable, i.e. $R_{Phys} = 0$. Therefore, using the inequalities (2.24), it is easy to observe that the outward and the inward fingers are formed for $R_{Chem} > 0$ and $R_{Chem} < 0$, respectively. It is observed that the critical values $R^*_{Chem,c}$ for different R_{Phys} have the same absolute values. However, for the stable ($R_{Phys} < 0$) and unstable ($R_{Phys} > 0$) physical fronts, the scenario is complex. For example, in the latter case, for $-R_{Phys} < R_{Chem} < R_{Phys}/\beta$, both the inward and outward fingering are simultaneously susceptible. With β increasing, the upper limit of this interval diminishes to zero and hence the length of this interval decreases. Contrary to that, in the former case, a stable displacement is expected for $R_{Phys}/\beta < R_{Chem} < -R_{Phys}$. Clearly, the effects of β on the critical parameter $R^*_{Chem,c}$ are significantly different when R_{Phys} changes sign (see figure 4). In summary, we observe that for the case of $\beta < 1$, the positive R_{Chem} systems are more unstable than the negative R_{Chem} ones for $R_{Phys} < 0$, and vice versa for $R_{Phys} > 0$.

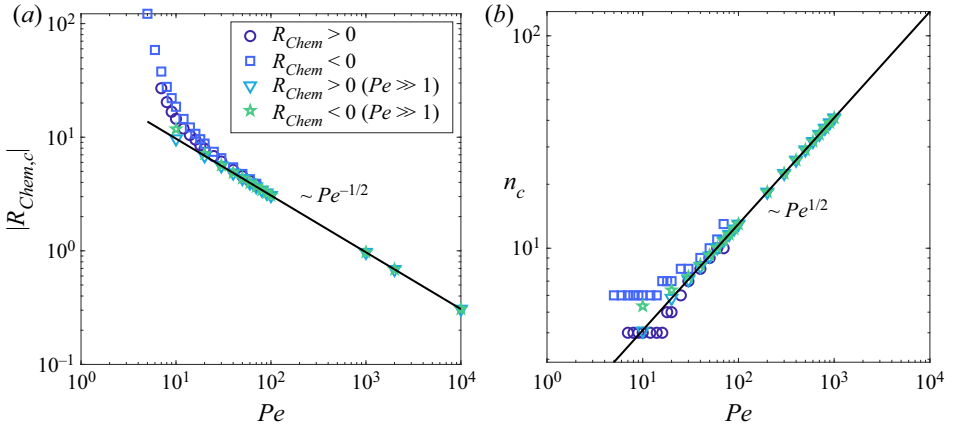

Figure 5. Linear stability results obtained for purely chemical systems ($R_{Phys} = 0$) with $\beta = 1$ and $Da^* \to \infty$ by solving (3.20) and (3.24) (for $Pe \gg 1$) using the numerical shooting method. Dependence of the critical parameters (*a*) $R_{Chem,c}$ and (*b*) n_c on Pe. The straight lines correspond to the asymptotic behaviour of these critical parameters in the limit of $Pe \to \infty$ obtained from the spectral analysis discussed in § 3.2.2.

This trend is reversed for the case of $\beta > 1$. Figure 4 implies that $R_{Chem,c}$ is a complex function of β, R_{Phys} and Pe.

Similarly, the critical values of R_{Chem} and n (i.e. $R_{Chem,c}$ and n_c) are obtained for (i) small and moderate values of Pe and (ii) $Pe \gg 1$ from the numerical shooting solutions of (3.19)–(3.21) and (3.23)–(3.25), respectively. Figure 5(*a*) depicts the variation of this critical parameter with Pe for small and moderate Pe as well as $Pe \gg 1$. It is observed that for small and moderate Pe (i.e. $Pe \lesssim 40$), the critical values for the finger formation in the outward-directing fingering system ($R_{Chem} > 0$) attain smaller values compared to those corresponding to the inward-directing fingering system ($R_{Chem} < 0$). This result is in qualitative agreement with NLS (cf. figures 8 and 9 of Sharma *et al.* (2019)). Corresponding to these critical values $R_{Chem,c}$, we also plot the critical wavenumber n_c in figure 5(*b*). This figure also depicts that for $Pe \gg 1$, $R_{Chem,c}$ are visually indistinguishable corresponding to the positive and the negative values of R_{Chem}, and they follow power-law behaviour $R_{Chem,c} \sim Pe^{-1/2}$ obtained in the $Pe \to \infty$ asymptotic limit. Again for $Pe \gg 1$, the critical wavenumbers follow the power-law relation obtained in the $Pe \to \infty$ asymptotic limit, i.e. $n_c \sim Pe^{1/2}$ as $Pe \gg 1$.

4. Nonlinear simulations

In § 3, we noted that R_{Phys} and R_{Chem} are the two important parameters controlling fingering instabilities. Although LSA indicates asymptotic instability for infinitesimal perturbations, to explore the nonlinearities of fingering instability numerical simulations of the full nonlinear problem are essential. Equations (2.5) are solved in the Cartesian coordinate system using COMSOL Multiphysics (COMSOL 2019).

It is worth mentioning that COMSOL Multiphysics has been much used in fluid dynamics research over the last decade (Campana & Carvalho 2014; Nejati, Dietzel & Hardt 2015; Nama, Huang & Costanzo 2017; Lerisson *et al.* 2020). COMSOL Multiphysics can be used as a high-level programming environment to create one's own implementation of problems in question as there may not exist any commercial module in COMSOL to solve such problems (Nama *et al.* 2017). Similarly in this study, we have also used

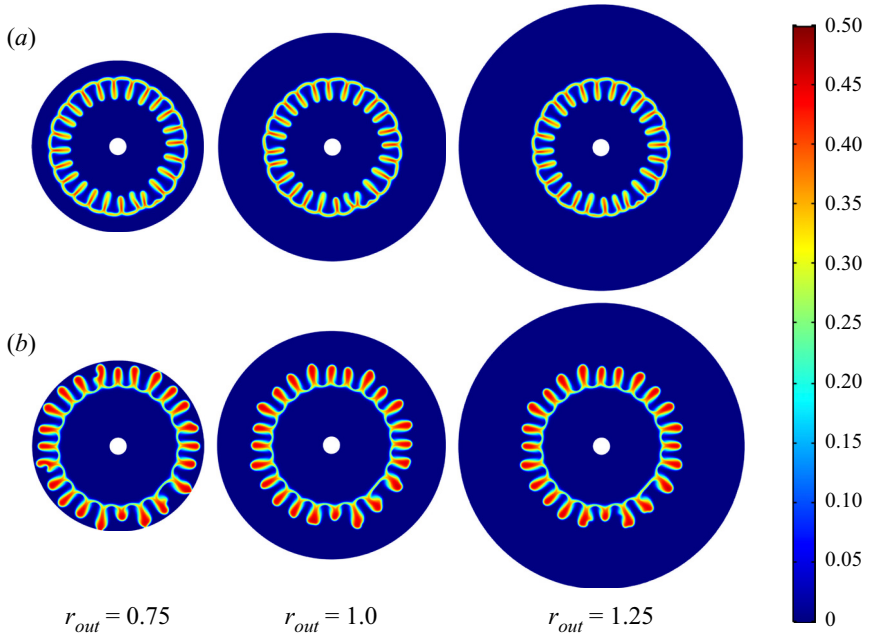

Figure 6. Effects of the domain boundary on concentration distribution of the product C at $\tau = 1$ for $Pe = 3000$, $Da = 100$, $\beta = 1$, $R_{Phys} = 0$ ($R_A = R_B = 0$), and $R_{Chem}(= -R_C) = -7$ (a) and $R_{Chem}(= -R_C) = 7$ (b).

COMSOL as a high-level programming environment. COMSOL has also been used recently to understand various physical aspects of miscible VF problems using the 'two-phase Darcy law' module of fluid flow interface (Sharma, Pramanik & Mishra 2016, 2017; Kumar & Mishra 2019). Although this module works well for understanding classical miscible VF problems, it cannot be used to include chemical reactions in a very convenient manner. Therefore, we adopt a different model formalism and model the fluid flow using the 'Darcy's law module', which is coupled with the 'transport of dilute species module' for the transport of the reactants A and B and the product C. The former describes a single-phase incompressible fluid dynamics in a porous medium, while the latter considers an advection–diffusion–reaction equation for a scalar species. These coupled nonlinear partial differential equations are solved in an annular region $\Omega = \{(x, y) : r_{in} \leqslant \sqrt{x^2 + y^2} \leqslant r_{out}\}$, where r_{out} is the outer radius of the annulus and r_{in} is the inner radius of the annulus. We impose the following initial and boundary conditions:

$$a(x, y, \tau = 0) = c(x, y, \tau = 0) = 0, b(x, y, \tau = 0) = \beta \quad \text{in } \Omega, \tag{4.1a}$$

$$a(x, y, \tau) = 1, b(x, y, \tau) = c(x, y, \tau) = 0, -\boldsymbol{u} \cdot \boldsymbol{n} = \frac{Q}{2\pi\sqrt{x^2 + y^2}} \quad \text{on } \partial\Omega_{in}, \tag{4.1b}$$

$$p(x, y, \tau) = 0, \boldsymbol{n} \cdot (Pe^{-1}\nabla c_i) = 0 (i = A, B, C) \quad \text{on } \partial\Omega_{out}, \tag{4.1c}$$

where $\boldsymbol{n}$ is the outward normal unit vector, and $\partial\Omega_{in} := \{(x, y) : \sqrt{x^2 + y^2} = r_{in}\}$, $\partial\Omega_{out} := \{(x, y) : \sqrt{x^2 + y^2} = r_{out}\}$, such that $\partial\Omega = \partial\Omega_{in} \cup \partial\Omega_{out}$ forms the boundary of the computational domain.

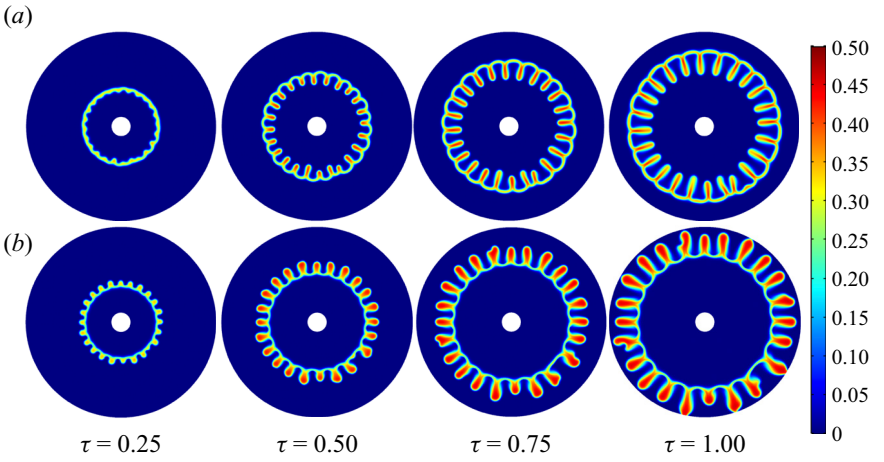

Figure 7. Temporal evolution of the concentration distribution of the product C for $Da = 100$, $Pe = 3000$, $\beta = 1$, $R_A = R_B = 0$, and $R_C = 7$ (a) and $R_C = -7$ (b).

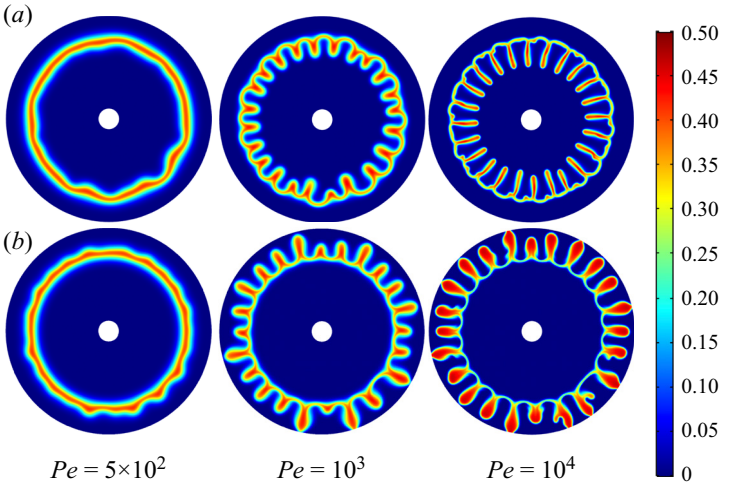

Figure 8. Effects of Péclet number Pe on the concentration distribution of the product C at $\tau = 1$ for $Da = 100$, $\beta = 1$, $R_A = R_B = 0$, and $R_C = 7$ (a) and $R_C = -7$ (b).

In order to make our numerical solutions independent of the size of the computational domain, we performed the numerical simulations for different domain sizes and found that for $r_{in} = 0.075$, fingering patterns are independent of the outer radius r_{out} when $r_{out} \geqslant 1$. This choice of the inner and the outer radii of the annulus is independent of the sign of R_{Chem} (see figure 6). For further validation of the numerical computations we reproduced figure 3 of Sharma *et al.* (2019).

We used first- or second-order, variable step size, backward differentiation formulae. At each time step, the system of nonlinear algebraic equations is linearized employing the Newton method, and the resulting linearized system is solved by the PARDISO direct solver which is fast, robust and multi-core capable. We used a scaled absolute tolerance

factor of 5×10^{-2} for the concentration and 1 for the pressure, and a relative tolerance of 10^{-4}.

A good qualitative agreement is observed using a free triangular mesh with the maximum and the minimum element sizes 10^{-2} and 5×10^{-4}, respectively (see figure 7). Further refinement of the finite element meshes does not change the fingering patterns significantly. Therefore, all the numerical simulations reported in this paper are performed in an annular domain with $r_{in} = 0.075$, $r_{out} > 1$ and maximum and minimum element sizes 10^{-2} and 5×10^{-4}, respectively. Further details of grid independence tests are given in Appendix E. We also successfully reproduced the effects of Pe on miscible fingering with pure chemical reaction, namely stronger instabilities for larger Pe (see figure 8). This is again in qualitative agreement with existing results (Sharma *et al.* 2019).

We notice that for sufficiently fast chemical reactions ($Da \sim O(10)$), the onset of fingering and the magnitude of the critical parameter $R_{Chem,c}$ for fingering are independent of the direction (inward versus outward) of the fingering. Sharma *et al.* (2019) observed similar effects of Da and reported that for $Da \gtrsim 80$, instability solely depends on the magnitude of the log-viscosity ratio R_C but not its sign. Therefore, throughout this paper, we choose $Da = 100$ in our NLS and that allows us to compare the NLS results with the linear stability results, which are obtained in the asymptotic limit $Da^* \to \infty$.

For simplicity, we restrict our analysis to $R_B = 0$. Therefore, our NLS results can be explained in terms of the two original dimensionless parameters R_A and R_C. However, for a qualitative comparison between the NLS and LSA, we present our results in terms of the newly constructed dimensionless parameters R_{Phys} and R_{Chem}. It is to be noted that the results presented here are qualitatively independent of choosing the combinations of R_A, R_B, R_C for obtaining R_{Phys} and R_{Chem}. A quantitative analysis of the effects of these parameters on the fingering dynamics will be the topic of future research.

4.1. *Effects of R_{Chem} and R_{Phys} on fingering dynamics*

In reactive systems, the effects of Da and Pe are well understood (Sharma *et al.* 2019). Very recently, it has been reported experimentally that a pH-sensitive clock reaction can induce VF even in a physically stable system, i.e. for $R_{Phys} < 0$ (Escala *et al.* 2019). Furthermore, the importance of the injection flow rate, the reactant species, the reactant concentrations, etc., on the pattern formation in precipitation reactions was experimentally captured (Schuszter & De Wit 2016; Schuszter *et al.* 2016*b*). When converted into our dimensionless formulation, these physicochemical effects correspond to the dimensionless parameters Pe, Da, R_{Phys}, R_{Chem} and β. Therefore, in order to explain such experimental findings numerically, we performed simulations and found that R_{Phys} and R_{Chem} are important parameters along with the reactants' concentration ratio β in such reactive systems (see figure 9). For both positive and negative R_{Chem} and all values of β, the displacement becomes more unstable as R_{Phys} increases and we experience a transition from physically stable systems ($R_{Phys} < 0$) to physically unstable systems ($R_{Phys} > 0$) through physically neutral systems ($R_{Phys} = 0$). For the physically stable and neutral systems, fingering at the inner and the outer sides of the product ring respectively for $R_{Chem} < 0$ and $R_{Chem} > 0$ distorts only one side of this ring, while the other side remains almost circular. However, for $R_{Phys} > 0$, the combined effects of physically and chemically unstable scenarios result in more complex fingering patterns and hence distort the product ring on both sides. Further, irrespective of the signs of R_{Phys} and R_{Chem} we observe, the higher the value of β, the stronger is the instability. These results are in qualitative agreement with the

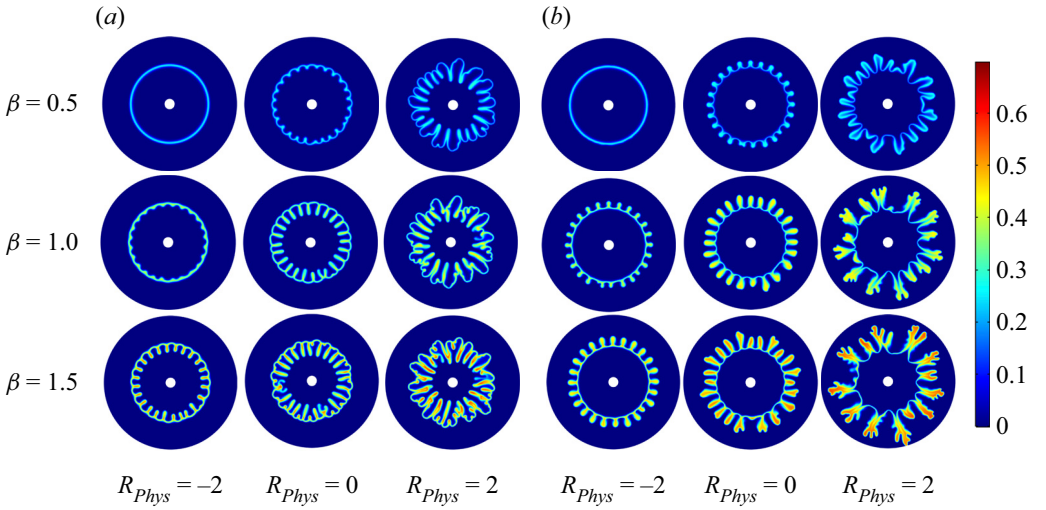

Figure 9. Concentration of product C at $\tau = 1$ for $Pe = 3000$, $Da = 100$, $\beta < 1$, $\beta = 1$, $\beta > 1$, and different values of $R_{Phys} = -(R_A - \beta R_B)$ with positive and negative $R_{Chem} = -(R_C - R_B - R_A)$. (*a*) For $R_{Chem} = -7$, we choose $(R_A, R_B, R_C) = (2, 0, 9)$, $(0, 0, 7)$ and $(-2, 0, 5)$ for $R_{Phys} = -2$, $R_{Phys} = 0$ and $R_{Phys} = 2$, respectively. (*b*) For $R_{Chem} = 7$, we choose $(R_A, R_B, R_C) = (2, 0, -5)$, $(0, 0, -7)$ and $(-2, 0, -9)$ for $R_{Phys} = -2$, $R_{Phys} = 0$ and $R_{Phys} = 2$, respectively.

predictions of the LSA and the physical mechanisms responsible for these effects are in line with those explained in § 3.3. In summary, the present NLS are helpful in explaining the complex precipitation pattern found experimentally (Nagatsu *et al.* 2014; Schuszter *et al.* 2016*a*,*b*; Schuszter & De Wit 2016).

4.2. *Effects of β on fingering dynamics*

We define the interfacial length of the product as

$$I(\tau) = \iint_{\Omega} |\nabla c| \, \mathrm{d}\Omega. \tag{4.2}$$

Figure 10 shows the interfacial length for $Da = 100$, $Pe = 3000$, $\beta = 0.5, 1, 1.5$ and different pairs of R_{Phys} and R_{Chem}. Figures 10(*a*) and 10(*c*) depict the cases of $R_{Chem} = 7$ and $R_{Chem} = -7$ for the physically unstable displacement ($R_{Phys} = 2$), whereas in figures 10(*b*) and 10(*d*) we show the cases of $R_{Chem} = 7$ and $R_{Chem} = -7$ for the physically stable displacement ($R_{Phys} = -2$). The maiden deviation of $I(\tau)$ corresponding to the non-zero R_{Phys} and R_{Chem} from the respective reference curve ($R_{Phys} = 0$ and $R_{Chem} = 0$) denotes the onset of instability. For a fixed pair of R_{Phys} and R_{Chem}, it is observed that not only is the interfacial length larger for a larger β, flow is more unstable and hence the instability sets in earlier for larger β. For $R_{Phys} = 2$, the onset of instability corresponding to $R_{Chem} = 7$ and -7 is almost identical for all three values of β considered. Here $R_{Phys} = -2$, $R_{Chem} = \pm 7$ and $\beta = 0.5$ correspond to stable displacements, which are also observed in figure 9. Whereas for $R_{Phys} = -2$ and $\beta = 1, 1.5$, the onset of outward fingers ($R_{Chem} = 7$) is earlier than that of inward fingers ($R_{Chem} = -7$), which is also consistent with figure 9.

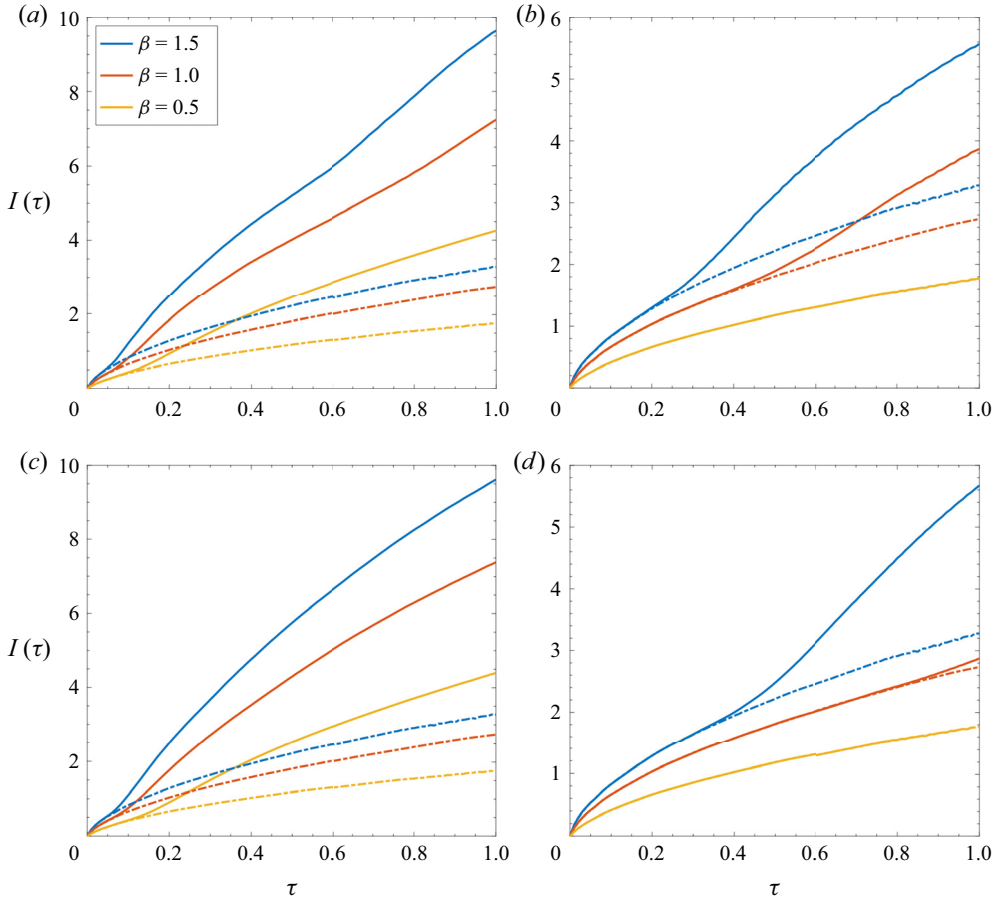

Figure 10. Evolution of interfacial length for $\beta = 0.5$, 1 and 1.5, $Da^* = 100$, $Pe = 3000$, and (*a*) $R_{Phys} = 2$, $R_{Chem} = 7$, (*b*) $R_{Phys} = -2$, $R_{Chem} = 7$, (*c*) $R_{Phys} = 2$, $R_{Chem} = -7$ and (*d*) $R_{Phys} = -2$, $R_{Chem} = -7$. The dash-dotted lines represent the corresponding stable displacement for $R_{Phys} = 0$, $R_{Chem} = 0$. The maiden deviation of each continuous line from the corresponding dash-dotted line denotes the onset of instability for the respective values of β.

5. Discussion and conclusions

The effects of chemical reaction on the onset and growth of the VF instability in a Hele-Shaw cell or in a homogeneous porous medium are analysed theoretically and numerically. The problem discussed in this paper offers rich parameter spaces spanned by several dimensionless parameters (β, R_A, R_B, R_C, Da and Pe).

We restrict the LSA to the asymptotic limit $Da^* \to \infty$. Linear stability analysis based on the numerical shooting method as well as spectral analysis suggested that the important parameters for the onset of VF instability are the Péclet number Pe, the Damkhöler number Da, the reactants' concentration ratio β and the log-viscosity parameters attributed to the physical and chemical effects, R_{Phys} and R_{Chem}, respectively. Furthermore, the effects of these parameters on the growth of the VF pattern were studied through NLS. In the present NLS, we identified shielding, tip-splitting and coalescence mechanisms, which are commonly found in experiments. In addition, we clearly showed that the physical parameters β and R_{Phys} make the fingering pattern more complex. These findings give

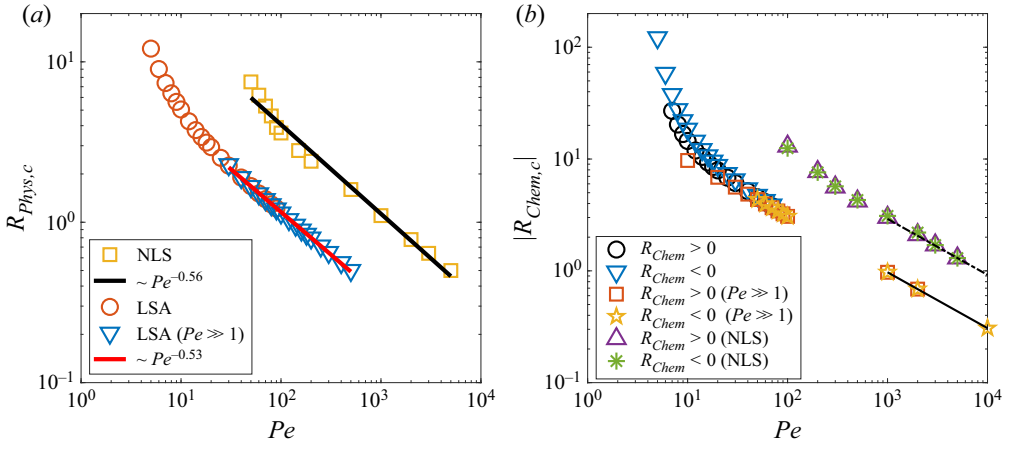

Figure 11. Dependence of the critical parameter (*a*) $R_{Phys,c}$ on Pe for the non-reactive system ($Da = 0$) and (*b*) $|R_{Chem,c}|$ on Pe for pure reactive systems ($R_{Phys} = 0$) with $\beta = 1$. In the reactive cases, LSA is performed for $Da^* \to \infty$; NLS are performed with $Da = 100$. For the reactive cases, the straight lines correspond to $\sim Pe^{-0.50}$.

important information for understanding experimental studies such as the precipitation pattern in confined geometries.

In the non-reactive cases (i.e. $Da = 0$), we compute the critical values of R_{Phys} (i.e. $R_{Phys,c}$) for different Pe from NLS and compare them with the corresponding values obtained from LSAs (see figure 11*a*). It is observed that corresponding to both LSA and NLS, $R_{Phys,c}$ decreases as Pe increases. Furthermore, this figure also depicts that for $Pe \sim O(10^2)$, $R_{Phys,c}$ obtained from the linear analysis (numerical shooting method) approaches $Pe \to \infty$ asymptotic behaviour (spectral analysis); namely $R_{Phys,c} \sim Pe^{-0.5}$ as $Pe \to \infty$. We fitted the numerically computed critical values for the entire range of Pe explored using a least-squares fit to a power law and we obtained $R_{Phys,c} \propto Pe^{-0.53}$. Note that the $Pe \to \infty$ asymptotic results were originally reported by Kim (2012). However, to make the current paper self-explanatory, we reproduced these results in terms of the notations used in this paper and compare them with the NLS. Interestingly, for $Pe \sim O(10^2)$, $R_{Phys,c}$ obtained from NLS also follows the same power-law behaviour barring a different pre-factor. Again, a least-squares fit of the numerically computed critical parameter to a power law in Pe gives a slightly different exponent: $R_{Phys,c} \propto Pe^{-0.56}$. This exponent is in agreement with a recent computational study that reported that the critical mobility ratio followed a power law in Pe with an exponent -0.55 (Sharma *et al.* 2020). The differences between the two power-law relations corresponding to LSA and NLS are attributed to the fact that the critical parameter $R_{Phys,c}$ in these two cases is calculated differently. In LSA, we defined $R_{Phys,c}$ as the minimum value of R_{Phys} for which at least one mode of the infinitesimal disturbances became unstable. Whereas, in NLS, $R_{Phys,c}$ is defined to be the smallest R_{Phys} for which interfacial length indicates fingering instability.

Next, we explore the dependence of the critical parameter $R_{Chem,c}$ on β. In the asymptotic limits $Pe \to \infty$ and $Da^* \to \infty$, the absolute values of $R_{Chem,c}$ obtained from linear analysis for positive and negative R_{Chem} are identical (see figure 4 in § 3.3). Therefore in these limits, we compute $R_{Chem,c}$ only for positive R_{Chem} and these are plotted for $0.3 \leqslant \beta \leqslant 3$ and $R_{Phys} = 0$ in figure 12. A least-squares fit depicts that $|R_{Chem,c}|$ decays with β as $|R_{Chem,c}| \sim \beta^{-0.50}$ as $Pe \to \infty$, $Da^* \to \infty$. However, for NLS there is no

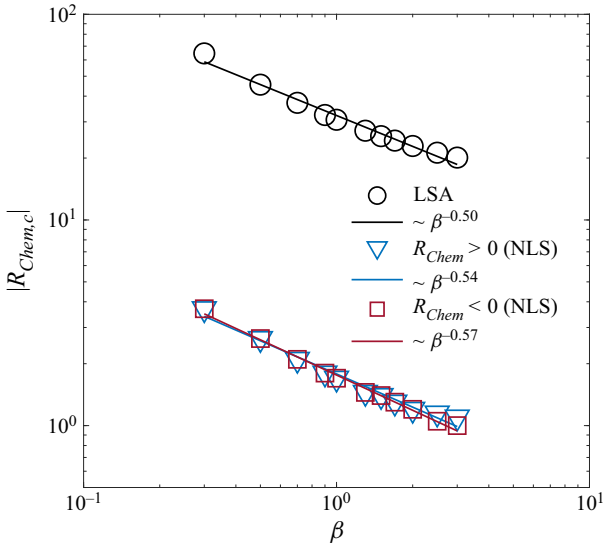

Figure 12. Dependence of the critical parameter $R_{Chem,c}$ on β captured from LSA for $Pe \to \infty$ and $Da^* \to \infty$, as well as NLS for fixed $Pe = 3000$ and $Da = 100$. For both LSA and NLS, we choose $R_{Phys} = 0$.

evidence that $R_{Chem,c}$ is identical for both positive and negative values of R_{Chem}. Therefore for NLS, we compute $|R_{Chem,c}|$ with $Pe = 3000$, $Da = 100$ and both positive and negative values of R_{Chem}. Least-squares fitting of the computed data yields: (i) for $R_{Chem} > 0$, $|R_{Chem,c}| \sim \beta^{-0.54}$ and (ii) for $R_{Chem} < 0$, $|R_{Chem,c}| \sim \beta^{-0.57}$. The power-law behaviour of $|R_{Chem,c}|$ in both linear and nonlinear regimes indicates qualitative agreement between the LSA and NLS results. The measured difference between the power-law exponents of LSA and NLS can be attributed to the different methods chosen to calculate the critical parameters in LSA and NLS as explained earlier. These observations led to our following analysis. We suitably rescaled $|R_{Chem,c}|$ with β for different values of β and explored the dependencies of the rescaled critical parameters on Pe.

We computed $|R_{Chem,c}|$ as a function of Pe for both positive and negative R_{Chem} and different values of β from both LSA and NLS. As expected, $|R_{Chem,c}|$ decreases as Pe increases. Similar to $R_{Phys,c}$, we obtain $|R_{Chem,c}| \sim Pe^{-0.5}$ as $Pe \to \infty$ and the pre-factors of these power-law relations are different for LSA and NLS. Furthermore, they depend on R_{Phys} and β. Figure 11(*b*) depicts the variations of $|R_{Chem,c}|$ with Pe for $R_{Phys} = 0$ and $\beta = 1$. However, when these critical values obtained from NLS are fitted for the entire range of Pe explored, we obtain a different power-law relation. It is observed that rescaled critical values $|R_{Chem,c}|\sqrt{\beta}$ collapse on a power law: $|R_{Chem,c}|\sqrt{\beta} \sim Pe^{-0.50}$ (LSA; see figure 13) and $|R_{Chem,c}|\sqrt{\beta} \sim Pe^{-0.55\pm0.01}$ (NLS; see figure 14).

In summary, we observed that larger values of β and Pe lead to stronger fingering motions. Although for small and moderate Pe positive and negative R_{Chem} exhibit slightly different critical values, for $Pe \geqslant 100$, the critical values corresponding to the positive and negative R_{Chem} are visually indistinguishable. Further quantitative analyses of different dimensionless parameter effects on the fingering motions await understanding and they are beyond the scope of this paper.

Finally, we note that the dynamics observed in this study can be explained in terms of the two mobility ratios R_{Phys} and R_{Chem} only in the limiting cases of $Da^* = 0$ and $Da^* \to \infty$. (Actually, for $Da^* = 0$, it is only R_{Phys} that is required to explain the dynamics.) In LSA,

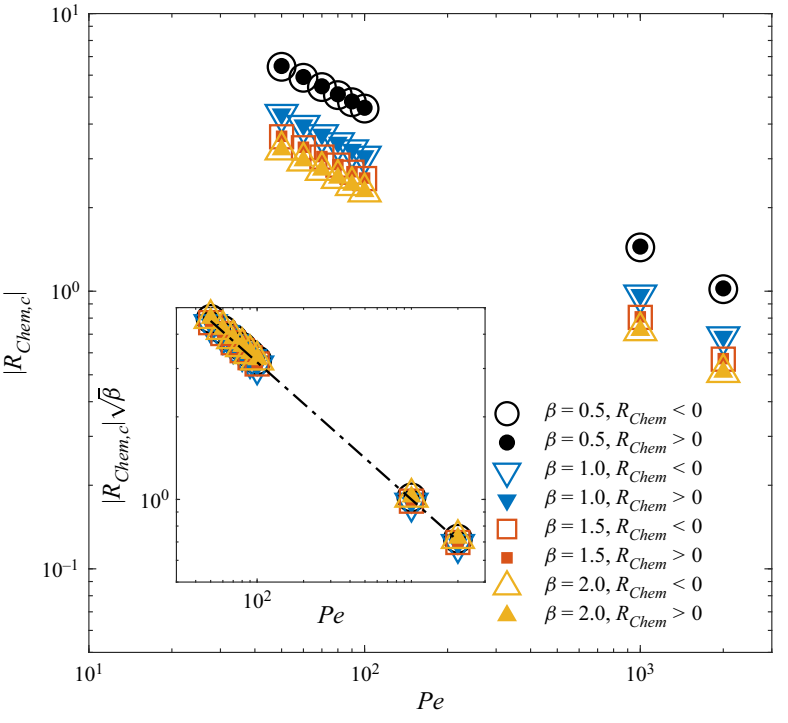

Figure 13. Dependence of the critical parameter $|R_{Chem,c}|$ on Pe, calculated for $Da^* \to \infty$ from LSA for different values of $\beta = 0.5$ (circle), 1.0 (down-pointing triangle), 1.5 (square), 2.0 (up-pointing triangle). Open symbols correspond to positive $R_{Chem,c}$, while filled symbols correspond to negative $R_{Chem,c}$. The inset shows the collapse of the data on a single master curve that follows a power law: $|R_{Chem,c}| \sim Pe^{-0.50}$.

this is evident from (3.14) and (B2). However, for finite but non-zero Da^*, we may need to specify R_A, R_B and R_C. Our NLS are carried out for $Da = 100$ and it is verified that the qualitative features of the observed fingering dynamics are independent of the choice of Da when Da is further increased. Therefore, our NLS are consistent with the $Da^* \to \infty$ limit. For $Da \sim O(10)$, which is beyond the scope of this paper, one must explore how the values of R_A, R_B and R_C affect the fingering dynamics, and further explore whether the same values of R_{Phys} and R_{Chem} obtained from different combinations of R_A, R_B and R_C and β can result in different fingering dynamics. The effects of Da on fingering dynamics in both the linear and nonlinear regimes are the topic of our ongoing research and will be reported elsewhere.

Funding. M.C.K. acknowledges the support of the Basic Science Research Program through the National Research Foundation of Korea (NRF) funded by the Ministry of Education (NRF-2018R1D1A3A03000703). S.P. acknowledges financial support through a Research Initiation Grant (RIG) from IITGN. M.M. acknowledges the financial support from SERB, Government of India through project grant no. MTR/2017/000283.

Declaration of interests. The authors report no conflict of interest.

Author ORCIDs.
Satyajit Pramanik https://orcid.org/0000-0001-8487-3551;
Vandita Sharma https://orcid.org/0000-0002-9348-2410;
Manoranjan Mishra https://orcid.org/0000-0001-9933-5828.

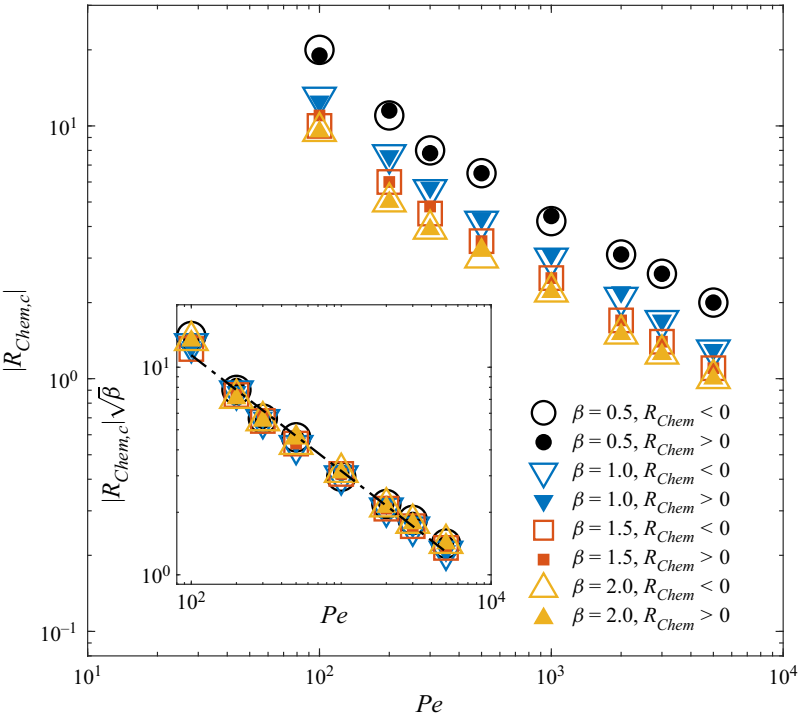

Figure 14. Dependence of the critical parameter $|R_{Chem,c}|$ on Pe, calculated for $Da = 100$ from NLS for different values of $\beta = 0.5$ (circle), 1.0 (down-pointing triangle), 1.5 (square), 2.0 (up-pointing triangle). Open symbols correspond to positive $R_{Chem,c}$, while filled symbols correspond to negative $R_{Chem,c}$. The inset shows the collapse of the data on a single master curve that follows a power law: $|R_{Chem,c}| \sim Pe^{-0.55\pm0.01}$.

Appendix A

Adding (2.9*a*) and (2.9*c*), and subtracting (2.9*b*) from (2.9*a*) we obtain

$$\frac{\partial}{\partial\tau}(a_0 + c_0) + \left(1 - \frac{1}{Pe}\right)\frac{1}{r}\frac{\partial}{\partial r}(a_0 + c_0) = \frac{1}{Pe}\frac{\partial^2}{\partial r^2}(a_0 + c_0), \tag{A1a}$$

$$\frac{\partial}{\partial\tau}(a_0 - b_0) + \left(1 - \frac{1}{Pe}\right)\frac{1}{r}\frac{\partial}{\partial r}(a_0 - b_0) = \frac{1}{Pe}\frac{\partial^2}{\partial r^2}(a_0 - b_0), \tag{A1b}$$

respectively. The associated boundary and initial conditions obtained from (2.10) are

$$a_0 - b_0 = 1, \quad a_0 + c_0 = 1, \text{ at } r = 0, \quad \tau > 0, \tag{A2a}$$

$$a_0 - b_0 = -\beta, \quad a_0 + c_0 = 0, \text{ at } r \to \infty, \quad \tau > 0, \tag{A2b}$$

$$a_0 - b_0 = -\beta, \quad a_0 + c_0 = 0, \text{ at } \tau = 0, \quad \forall\, r. \tag{A2c}$$

Define a new variable ϕ_0 as follows:

$$\phi_0 = \frac{a_0 - b_0 + \beta}{1 + \beta} \equiv a_0 + c_0. \tag{A3}$$

Then, ϕ_0 satisfies the following initial boundary value problem:

$$\frac{\partial \phi_0}{\partial \tau} + \left(1 - \frac{1}{Pe}\right)\frac{1}{r}\frac{\partial \phi_0}{\partial r} = \frac{1}{Pe}\frac{\partial^2 \phi_0}{\partial r^2}, \tag{A4a}$$

$$\phi_0(r, 0) = 0, \quad \phi_0(0, \tau) = 1 \quad \text{and} \quad \phi_0(\infty, \tau) = 0. \tag{A4b}$$

Appendix B. Linear stability analysis for the non-reactive case

For the non-reactive case, i.e. $Da^* = 0$, in which $c_1(\xi, \tau) = 0$, (3.4) and (3.7) give

$$(a_1, b_1) = (\phi_1, -\beta\phi_1). \tag{B1}$$

Therefore, the stability equation (3.8*a*) reads

$$\frac{\partial}{\partial \xi}\left(\xi \frac{\partial \psi_1}{\partial \xi}\right) - R_{Phys}\frac{\mathrm{d}\phi_0}{\mathrm{d}\xi}\xi\frac{\partial \psi_1}{\partial \xi} + \frac{1}{4\xi}\frac{\partial^2 \psi_1}{\partial \theta^2} = \frac{R_{Phys}}{4\xi}\frac{\partial^2 \phi_1}{\partial \theta^2}, \tag{B2}$$

whereas (3.10*a*) reduces to

$$\frac{\partial^2 \psi_1^*}{\partial \zeta^2} - R_{Phys}\frac{\mathrm{d}\phi_0}{\mathrm{d}\zeta}\frac{\partial \psi_1^*}{\partial \zeta} + \frac{1}{Pe}\frac{\partial^2 \psi_1^*}{\partial \theta^2} = +\frac{R^*_{Phys}}{Pe}\frac{\partial^2 \phi_1}{\partial \theta^2} + O(Pe^{-1/2}) \quad Pe \to \infty. \tag{B3}$$

Applying the normal mode decompositions discussed in § 3.2, these equations further simplify to

$$\frac{\mathrm{d}}{\mathrm{d}\xi}\left(\xi\frac{\mathrm{d}\Psi}{\mathrm{d}\xi}\right) - R_{Phys}\frac{\mathrm{d}\phi_0}{\mathrm{d}\xi}\xi\frac{\mathrm{d}\Psi}{\mathrm{d}\xi} - \frac{n^2}{4\xi}\Psi = -R_{Phys}\frac{n^2}{4\xi}\Phi \tag{B4}$$

and

$$\left(\frac{\mathrm{d}^2}{\mathrm{d}\zeta^2} - R_{Phys}\frac{\mathrm{d}\phi_0}{\mathrm{d}\zeta}\frac{\mathrm{d}}{\mathrm{d}\zeta} - \frac{n^2}{Pe}\right)\Psi^* = -R^*_{Phys}\frac{n^2}{Pe}\Phi \quad Pe \to \infty, \tag{B5}$$

respectively.

Appendix C. Analytic solutions of the spectral analysis equations

Solving (3.31*a*) and (3.31*b*), the following recurrence relation can be obtained:

$$\psi_i^-(k, \zeta) = k^2\left[\psi_{i-2}^-(k, \zeta) - (R^*_{Phys} - \beta R^*_{Chem})\phi_{i-2}(\zeta)\right] + \frac{k}{2}(1+\beta)R^*_{Chem}\mathrm{e}^{k(\zeta-\zeta_R)}(\phi_{n-1}(\zeta_R) - k\phi_{n-2}(\zeta_R)), \tag{C1}$$

with

$$\psi_0^-(k, \zeta) = \frac{k}{4}\sqrt{\pi}\mathrm{e}^{k^2/4}\left[(R^*_{Phys} - \beta R^*_{Chem})\left\{\mathrm{e}^{k\zeta}\,\mathrm{erfc}\left(\zeta + \frac{k}{2}\right) + \mathrm{e}^{-k\zeta}\,\mathrm{erfc}\left(-\zeta + \frac{k}{2}\right)\right\} + (1+\beta)R^*_{Chem}\mathrm{e}^{k\zeta}\,\mathrm{erfc}\left(\zeta_R + \frac{k}{2}\right)\right], \quad \zeta \leqslant \zeta_R, \tag{C2a}$$

$$\psi_1^-(k, \zeta) = -\frac{k}{2}\mathrm{e}^{k^2/4}\left[(R^*_{Phys} - \beta R^*_{Chem})\frac{k}{2}\sqrt{\pi}\left\{\mathrm{e}^{k\zeta}\,\mathrm{erfc}\left(\zeta + \frac{k}{2}\right) + \mathrm{e}^{-k\zeta}\,\mathrm{erfc}\left(-\zeta + \frac{k}{2}\right)\right\} - (1+\beta)R^*_{Chem}\mathrm{e}^{k\zeta}\left\{\mathrm{e}^{-(\zeta_R + k/2)^2} - \frac{k}{2}\sqrt{\pi}\,\mathrm{erfc}\left(\zeta_R + \frac{k}{2}\right)\right\}\right], \quad \zeta \leqslant \zeta_R, \tag{C2b}$$

and

$$\psi_n^+(k,\zeta) = k^2\left[\psi_{n-2}^+(k,\zeta) - (R^*_{Phys}+R^*_{Chem})\phi_{n-2}(\zeta)\right] + \frac{k}{2}(1+\beta)R^*_{Chem}\mathrm{e}^{-k(\zeta-\zeta_R)}(\phi_{n-1}(\zeta_R)+k\phi_{n-2}(\zeta_R)), \tag{C3}$$

with

$$\psi_0^+(k,\zeta) = \frac{k}{4}\sqrt{\pi}\mathrm{e}^{k^2/4}\left[(R^*_{Phys}+R^*_{Chem})\left\{\mathrm{e}^{k\zeta}\mathrm{erfc}\left(\zeta+\frac{k}{2}\right)+\mathrm{e}^{-k\zeta}\mathrm{erfc}\left(-\zeta+\frac{k}{2}\right)\right\} - (1+\beta)R^*_{Chem}\mathrm{e}^{-k\zeta}\mathrm{erfc}\left(-\zeta_R+\frac{k}{2}\right)\right], \quad \zeta \geqslant \zeta_R, \tag{C4a}$$

$$\psi_1^+(k,\zeta) = -\frac{k}{2}\mathrm{e}^{k^2/4}\left[(R^*_{Phys}+R^*_{Chem})\frac{k}{2}\sqrt{\pi}\left\{\mathrm{e}^{k\zeta}\mathrm{erfc}\left(\zeta+\frac{k}{2}\right)-\mathrm{e}^{-k\zeta}\mathrm{erfc}\left(-\zeta+\frac{k}{2}\right)\right\} - (1+\beta)R^*_{Chem}\mathrm{e}^{-k\zeta}\left\{\mathrm{e}^{-(-\zeta_R+k/2)^2}-\frac{k}{2}\sqrt{\pi}\mathrm{erfc}\left(-\zeta_R+\frac{k}{2}\right)\right\}\right], \quad \zeta \geqslant \zeta_R. \tag{C4b}$$

For the non-reactive system ($Da^* = 0$), spectral analysis requires one to solve (B5) for the limiting cases of $Pe \to \infty$, $R_{Phys} \ll 1$, but finite R^*_{Phys}. In this limit, this equation reduces to

$$\frac{\mathrm{d}^2\psi_i}{\mathrm{d}\zeta^2} - k^2\psi_i^- = -R^*_{Phys}k^2\mathrm{e}^{-\zeta^2}H_i(\zeta). \tag{C5}$$

Solving this, we obtain the following relation:

$$\psi_i(k,\zeta) = k^2[\psi_{i-2}(k,\zeta) - R^*_{Phys}\phi_{i-2}(\zeta)], \tag{C6}$$

with

$$\psi_0(\zeta,k) = \sqrt{\pi}\frac{k}{4}\mathrm{e}^{k^2/4}R^*_{Phys}\left[\mathrm{e}^{k\zeta}\mathrm{erfc}\left(\zeta+\frac{k}{2}\right)+\mathrm{e}^{-k\zeta}\mathrm{erfc}\left(-\zeta+\frac{k}{2}\right)\right], \tag{C7a}$$

$$\psi_1(\zeta,k) = \frac{k}{4}\mathrm{e}^{k^2/4}R^*_{Phys}\left[\mathrm{e}^{k\zeta}\left\{2\mathrm{e}^{-(\zeta+k/2)^2}-k\sqrt{\pi}\mathrm{erfc}\left(\zeta+\frac{k}{2}\right)\right\} -\mathrm{e}^{-k\zeta}\left\{2\mathrm{e}^{-(-\zeta+k/2)^2}-k\sqrt{\pi}\mathrm{erfc}\left(-\zeta+\frac{k}{2}\right)\right\}\right]. \tag{C7b}$$

Appendix D

Using the map $\zeta \mapsto -\zeta$, (3.36*b*) and (3.37*b*) take the forms

$$\frac{\mathrm{d}^2\psi_{i,n}^+}{\mathrm{d}\zeta^2} - k^2\psi_{i,n}^+ = -k^2\left(R^*_{Phys}+\left|R^*_{Chem}\right|\right)\mathrm{e}^{-\zeta^2}H_i(-\zeta) \quad \text{for } \zeta < 0, \tag{D1a}$$

$$\frac{\mathrm{d}^2\psi_{i,p}^+}{\mathrm{d}\zeta^2} - k^2\psi_{i,p}^+ = -k^2\left(R^*_{Phys}-\left|R^*_{Chem}\right|\right)\mathrm{e}^{-\zeta^2}H_i(-\zeta) \quad \text{for } \zeta < 0, \tag{D1b}$$

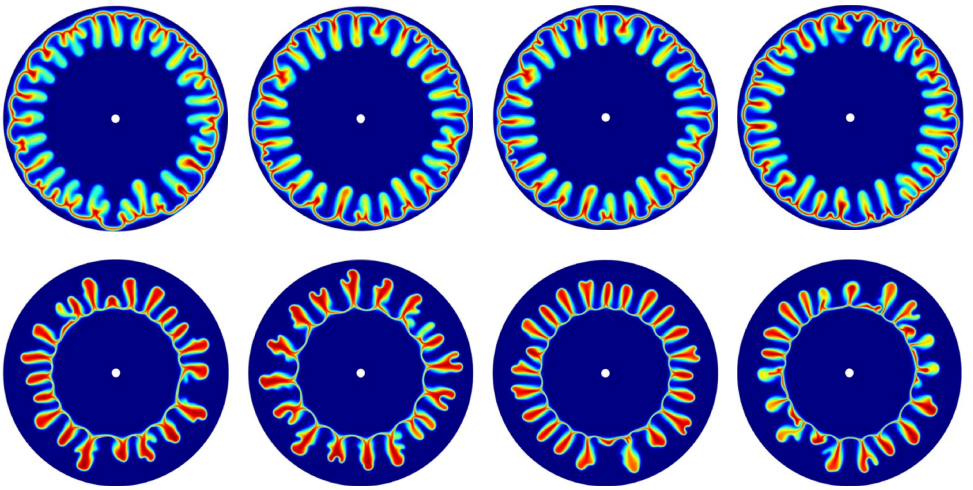

Figure 15. Concentration fields of the product C for the parameters $Pe = 3000$, $Da = 100$, $R_A = R_B = 0$. In the upper panel, $R_C = 7$, $\tau = 10$; in the lower panel, $R_C = -7$, $\tau = 5$. The variable time step backward differentiation formula was employed and relative tolerance was set to 10^{-4}.

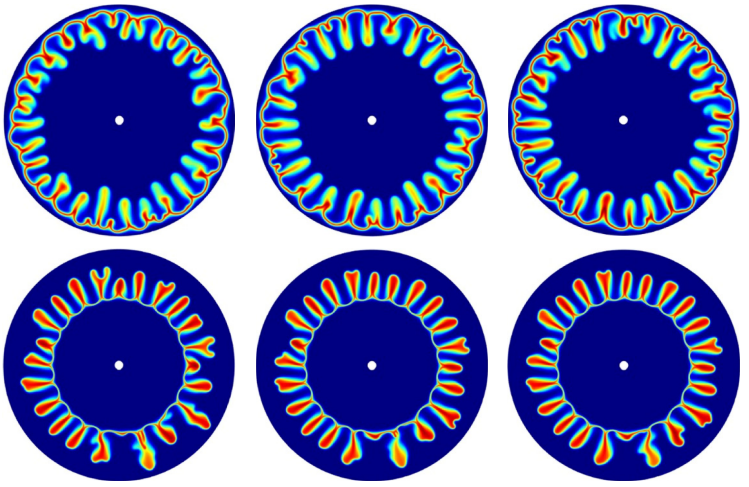

Figure 16. Concentration fields of the product C for the parameters $Pe = 3000$, $Da = 100$, $R_A = R_B = 0$. In the upper panel, $R_C = 7$, $\tau = 10$; in the lower panel, $R_C = -7$, $\tau = 5$. The number of elements used in these simulations is 375 484.

respectively. For $H_i(-\zeta) = -H_i(\zeta)$ (D1*a*) and (D1*b*) become

$$\frac{\mathrm{d}^2(-\psi_{i,n}^+)}{\mathrm{d}\zeta^2} - k^2(-\psi_{i,n}^+) = -k^2\left(R^*_{Phys} + \left|R^*_{Chem}\right|\right)\mathrm{e}^{-\zeta^2}H_i(\zeta) \quad \text{for } \zeta < 0, \qquad \text{(D2}a\text{)}$$

$$\frac{\mathrm{d}^2(-\psi_{i,p}^+)}{\mathrm{d}\zeta^2} - k^2(-\psi_{i,p}^+) = -k^2\left(R^*_{Phys} - \left|R^*_{Chem}\right|\right)\mathrm{e}^{-\zeta^2}H_i(\zeta) \quad \text{for } \zeta < 0, \qquad \text{(D2}b\text{)}$$

Spatial resolution	Number of elements	Maximum element size	Minimum element size
Coarser	96 646	2.0×10^{-2}	1×10^{-3}
Coarse	170 130	1.5×10^{-2}	5×10^{-4}
Fine	375 484	1.0×10^{-2}	5×10^{-4}
Finer	663 008	7.5×10^{-3}	5×10^{-4}

Table 1. Detailed explanation of mesh structures employed for the case of $Pe = 3000$, $Da = 100$, $R_A = R_B = 0$ and $R_C = 7$.

Relative tolerance	Initial time step	maximum time step
10^{-3}	2.0894×10^{-5}	1.8420×10^{-2}
10^{-4}	2.1279×10^{-6}	9.5192×10^{-3}
10^{-5}	2.1292×10^{-7}	3.1013×10^{-3}

Table 2. Time steps used in the case of $Pe = 3000$, $Da = 100$, $R_A = R_B = 0$ and $R_C = 7$. The number of element used is 375 484 (fine).

which are identical to (3.37*a*) and (3.36*a*), respectively, for $-\psi_{i,n}^{+} = \psi_{i,p}^{-}$ and $-\psi_{i,p}^{+} = \psi_{i,n}^{-}$. Similarly for $H_i(-\zeta) = H_i(\zeta)$, we can show that $\psi_{i,n}^{+} = \psi_{i,p}^{-}$ and $\psi_{i,p}^{+} = \psi_{i,n}^{-}$.

Appendix E. Further details of COMSOL simulations

The snapshots of the concentration field at $\tau = 10$ (for $R_C = 7$) and $\tau = 5$ (for $R_C = -7$) corresponding to different spatiotemporal resolutions as well as different relative tolerances are plotted in figures 15 and 16. These show that there are no significant qualitative changes in the observed nonlinear dynamics and pattern formation. Therefore, we fixed the spatial resolution corresponding to 'fine' mesh and the relative tolerance to 10^{-4} in all the simulations throughout this paper. Table 1 and Table 2 show the data related to the grid independence studies carried out for a reference case in this paper.

References

Al-Gwaiz, M.A. 2008 *Sturm-Liouville Theory and its Applications*. Springer-Verlag.

Balog, E., Bittmann, K., Schwarzenberger, K., Eckert, K., De Wit, A. & Schuszter, G. 2019 Influence of microscopic precipitate structures on macroscopic pattern formation in reactive flows in a confined geometry. *Phys. Chem. Chem. Phys.* **21**, 2910–2918.

Ben, Y., Demekhin, E.A. & Chang, H.-C. 2002 A spectral theory for small-amplitude miscible fingering. *Phys. Fluids* **14** (3), 999–1010.

Brau, F. & De Wit, A. 2020 Influence of rectilinear vs radial advection on the yield of $A + B \rightarrow C$ reaction fronts: a comparison. *J. Chem. Phys.* **152** (5), 054716.

Brau, F., Schuszter, G. & De Wit, A. 2017 Flow control of $A + B \rightarrow C$ fronts by radial injection. *Phys. Rev. Lett.* **118**, 134101.

Campana, D.M. & Carvalho, M.S. 2014 Liquid transfer from single cavities to rotating rolls. *J. Fluid Mech.* **747**, 545–571.

Cardenas, M.B., *et al.*2019 Submarine groundwater and vent discharge in a volcanic area associated with coastal acidification. *Geophys. Res. Lett.* e2019GL085730.

Chandrasekhar, S. 2013 *Hydrodynamic and Hydromagnetic Stability*. Courier Corporation.

Chung, D.-W., Shearing, P.R., Brandon, N.P., Harris, S.J. & García, R.E. 2014 Particle size polydispersity in Li-ion batteries. *J. Electrochem. Soc.* **161** (3), A422–A430.

COMSOL 2019 v. 5.4 COMSOL AB.

DAVIT, Y., BYRNE, H., OSBORNE, J., PITT-FRANCIS, J., GAVAGHAN, D. & QUINTARD, M. 2013 Hydrodynamic dispersion within porous biofilms. *Phys. Rev.* E **87** (1), 012718.

DE WIT, A. 2016 Chemo-hydrodynamic patterns in porous media. *Phil. Trans. R. Soc.* A **374** (2078), 20150419.

DE WIT, A. 2020 Chemo-hydrodynamic patterns and instabilities. *Annu. Rev. Fluid Mech.* **52**, 531–555.

DRAZIN, P.G. & REID, W.H. 2004 *Hydrodynamic Stability*. Cambridge University Press.

ESCALA, D.M., DE WIT, A., CARBALLIDO-LANDEIRA, J. & MUÑUZURI, A.P. 2019 Viscous fingering induced by a pH-sensitive clock reaction. *Langmuir* **35** (11), 4182–4188.

GÉRARD, T. & DE WIT, A. 2009 Miscible viscous fingering induced by a simple $A + B \rightarrow C$ chemical reaction. *Phys. Rev.* E **79** (1), 016308.

HEJAZI, S.H., TREVELYAN, P.M.J., AZAIEZ, J. & DE WIT, A. 2010 Viscous fingering of a miscible reactive $a + b \rightarrow c$ interface: a linear stability analysis. *J. Fluid Mech.* **652**, 501–528.

HILL, S. 1952 Channeling in packed columns. *Chem. Engng Sci.* **1** (6), 247–253.

HOMSY, G.M. 1987 Viscous fingering in porous media. *Annu. Rev. Fluid Mech.* **19**, 271–311.

HUPPERT, H.E. & NEUFELD, J.A. 2014 The fluid mechanics of carbon dioxide sequestration. *Annu. Rev. Fluid Mech.* **46** (1), 255–272.

KIM, M.C. 2012 Onset of radial viscous fingering in a Hele-Shaw cell. *Korean J. Chem. Engng* **29** (12), 1688–1694.

KIM, M.C. 2014 Effect of the irreversible $A + B \rightarrow C$ reaction on the onset and the growth of the buoyancy-driven instability in a porous medium. *Chem. Engng Sci.* **112**, 56–71.

KIM, M.C. 2018 Double diffusive effects on radial fingering in a porous medium or a Hele-Shaw cell. *Korean J. Chem. Engng* **35** (2), 364–374.

KIM, M.C. & CHOI, C.K. 2011 The stability of miscible displacement in porous media: nonmonotonic viscosity profiles. *Phys. Fluids* **23** (8), 084105.

KUMAR, A. & MISHRA, M. 2019 Boundary effects on the onset of miscible viscous fingering in a Hele-Shaw flow. *Phys. Rev. Fluids* **4**, 104004.

LERISSON, G., LEDDA, P.G., BALESTRA, G. & GALLAIRE, F. 2020 Instability of a thin viscous film flowing under an inclined substrate: steady patterns. *J. Fluid Mech.* **898**, A6.

MCDOWELL, A., ZARROUK, S.J. & CLARKE, R. 2016 Modelling viscous fingering during reinjection in geothermal reservoirs. *Geothermics* **64**, 220–234.

NAGATSU, Y & DE WIT, A. 2011 Viscous fingering of a miscible reactive $A + B \rightarrow C$ interface for an infinitely fast chemical reaction: nonlinear simulations. *Phys. Fluids* **23** (4), 043103.

NAGATSU, Y., ISHII, Y., TADA, Y. & DE WIT, A. 2014 Hydrodynamic fingering instability induced by a precipitation reaction. *Phys. Rev. Lett.* **113**, 024502.

NAGATSU, Y., MATSUDA, K., KATO, Y. & TADA, Y. 2007 Experimental study on miscible viscous fingering involving viscosity changes induced by variations in chemical species concentrations due to chemical reactions. *J. Fluid Mech.* **571**, 475–493.

NAMA, N., HUANG, T.J. & COSTANZO, F. 2017 Acoustic streaming: an arbitrary Lagrangian–Eulerian perspective. *J. Fluid Mech.* **825**, 600–630.

NEJATI, I., DIETZEL, M. & HARDT, S. 2015 Conjugated liquid layers driven by the short-wavelength Bénard–Marangoni instability: experiment and numerical simulation. *J. Fluid Mech.* **783**, 46–71.

PATERSON, L. 1981 Radial fingering in a Hele Shaw cell. *J. Fluid Mech.* **113**, 513–529.

PRITCHARD, D. 2004 The instability of thermal and fluid fronts during radial injection in a porous medium. *J. Fluid Mech.* **508**, 133–163.

RANA, C., PRAMANIK, S., MARTIN, M., DE WIT, A & MISHRA, M. 2019 Influence of langmuir adsorption and viscous fingering on transport of finite size samples in porous media. *Phys. Rev. Fluids* **4** (10), 104001.

RIAZ, A. & MEIBURG, E. 2003*a* Radial source flows in porous media: linear stability analysis of axial and helical perturbations in miscible displacements. *Phys. Fluids* **15** (4), 938–946.

RIAZ, A. & MEIBURG, E. 2003*b* Three-dimensional miscible displacement simulations in homogeneous porous media with gravity override. *J. Fluid Mech.* **494**, 95–117.

RIAZ, A., PANKIEWITZ, C. & MEIBURG, E. 2004 Linear stability of radial displacements in porous media: influence of velocity-induced dispersion and concentration-dependent diffusion. *Phys. Fluids* **16** (10), 3592–3598.

SAFFMAN, P.G. & TAYLOR, G.I. 1958 The penetration of a fluid into a porous medium or Hele-Shaw cell containing a more viscous liquid. *Proc. R. Soc. Lond.* A *Math. Phys. Sci.* **245** (1242), 312–329.

SCHUSZTER, G., BRAU, F. & DE WIT, A. 2016*a* Calcium carbonate mineralization in a confined geometry. *Environ. Sci. Technol. Lett.* **3** (4), 156–159.

SCHUSZTER, G., BRAU, F. & DE WIT, A. 2016*b* Flow-driven control of calcium carbonate precipitation patterns in a confined geometry. *Phys. Chem. Chem. Phys.* **18**, 25592–25600.

SCHUSZTER, G. & DE WIT, A. 2016 Comparison of flow-controlled calcium and barium carbonate precipitation patterns. *J. Chem. Phys.* **145** (22), 224201.

SHARMA, V., NAND, S., PRAMANIK, S., CHEN, C.-Y. & MISHRA, M. 2020 Control of radial miscible viscous fingering. *J. Fluid Mech.* **884**, A16.

SHARMA, V., PRAMANIK, S., CHEN, C.-Y. & MISHRA, M. 2019 A numerical study on reaction-induced radial fingering instability. *J. Fluid Mech.* **862**, 624–638.

SHARMA, V., PRAMANIK, S. & MISHRA, M. 2016 Fingering instabilities in variable viscosity miscible fluids: radial source flow. In *Proceedings of the 2016 COMSOL Conference in Bangalore*.

SHARMA, V., PRAMANIK, S. & MISHRA, M. 2017 Dynamics of a highly viscous circular blob in homogeneous porous media. *Fluids* **2** (4), 32.

TAN, C.T. & HOMSY, G.M. 1987 Stability of miscible displacements in porous media: radial source flow. *Phys. Fluids* **30** (5), 1239–1245.

TÓTH, Á., SCHUSZTER, G., DAS, N.P., LANTOS, E., HORVÁTH, D., DE WIT, A. & BRAU, F. 2020 Effects of radial injection and solution thickness on the dynamics of confined $A + B \rightarrow C$ chemical fronts. *Phys. Chem. Chem. Phys.* **22** (18), 10278–10285.

TREVELYAN, P.M.J. & WALKER, A.J. 2018 Asymptotic properties of radial $A + B \rightarrow C$ reaction fronts. *Phys. Rev.* E **98**, 032118.

WELTY, C., KANE, A.C. & KAUFFMAN, L.J. 2003 Stochastic analysis of transverse dispersion in density-coupled transport in aquifers. *Water Resour. Res.* **39** (6), 1150.

YORTSOS, Y.C. 1987 Stability of displacement processes in porous media in radial flow geometries. *Phys. Fluids* **30** (10), 2928–2935.